Available online at www.sciencedirect.com

ScienceDirect

Geochimica et Cosmochimica Acta 72 (2008) 1801–1823

Geochimica et Cosmochimica Acta

www.elsevier.com/locate/gca

Isotopic and element exchange during serpentinization and metasomatism at the Atlantis Massif (MAR 30°N): Insights from B and Sr isotope data

Chiara Boschi[a,b], Andrea Dini[b], Gretchen L. Früh-Green[a,*], Deborah S. Kelley[c]

[a] *Institute for Mineralogy and Petrology, ETH Zurich, CH-8092 Zurich, Switzerland*
[b] *Istituto di Geoscienze e Georisorse, CNR, Pisa, Italy*
[c] *University of Washington, School of Oceanography, Seattle, WA, USA*

Received 21 June 2007; accepted in revised form 14 January 2008; available online 31 January 2008

Abstract

The Lost City hydrothermal system at the southern Atlantis Massif (Mid-Atlantic Ridge, 30°N) provides a natural laboratory for studying serpentinization processes, the temporal evolution of ultramafic-hosted hydrothermal systems, and alteration conditions during formation and emplacement of an oceanic core complex. Here we present B, O, and Sr isotope data to investigate fluid/rock interaction and mass transfer during detachment faulting and exhumation of lithospheric sequences within the Atlantis Massif. Our data indicate that extensive serpentinization was a seawater-dominated process that occurred predominately at temperatures of 150–250 °C and at high integrated W/R ratios that led to a marked boron enrichment (34–91 ppm). Boron removal from seawater during serpentinization is positively correlated with changes in $\delta^{11}B$ (11–16‰) but shows no correlation with O-isotope composition. Modeling indicates that B concentrations and isotope values of the serpentinites are controlled by transient temperature–pH conditions. In contrast to prior studies, we conclude that low-temperature marine weathering processes are insignificant for boron geochemistry of the Atlantis Massif serpentinites. Talc- and amphibole-rich fault rocks formed within a zone of detachment faulting at temperatures of approximately 270–350 °C and at low W/R ratios. Talc formation in ultramafic domains in the massif was subsequent to an early stage of serpentinization and was controlled by the access of Si-rich fluids derived through seawater–gabbro interactions. Replacement of serpentine by talc resulted in boron loss and significant lowering of $\delta^{11}B$ values (9–10‰), which we model as the product of progressive extraction of boron. Our study provides new constraints on the boron geochemical cycle at oceanic spreading ridges and suggests that serpentinization associated with ultramafic-hosted hydrothermal systems may have important implications for the behavior of boron in subduction zone settings.

1. INTRODUCTION

Hydrothermal circulation at mid-ocean ridges and flank environments plays a significant role in cycling energy and mass between the lithosphere and the oceans (e.g., Lister, 1972; Fisher and Becker, 2000; Wheat and Mottl, 2004). It is estimated that water volumes equivalent to the entire volume of the ocean circulates through the oceanic crust in less than 20 My (German and Von Damm, 2003; Wheat and Mottl, 2004). In turn, chemical and isotopic exchange during hydrothermal alteration of the oceanic crust influences the geochemistry of magmatism at convergent boundaries where subduction zone processes release volatiles and mobile elements from the altered oceanic lithosphere into the mantle wedge (Forneris and Holloway, 2003; Hattori and Guillot, 2003; Scambelluri et al., 2004; Tenthorey and Hermann, 2004; Savov et al., 2005a,b; Alt and Shanks, 2006; Fryer et al., 2006; Savov et al., 2007). Thus, the study

---

[*] Corresponding author. Fax: +41 44 632 1636.
E-mail address: frueh@erdw.ethz.ch (G.L. Früh-Green).

0016-7037/$ - see front matter © 2008 Elsevier Ltd. All rights reserved.
doi:10.1016/j.gca.2008.01.013

of isotopic and element exchange (and related mineralogical–textural variations) that occur during fluid–rock interaction of the oceanic lithosphere is central to numerous Earth and paleo-environmental studies.

Thirty years of investigations of hydrothermal vents at mid-ocean ridges (e.g., Edmond et al., 1979; Campbell et al., 1988; German and Von Damm, 2003) have yielded significant observational and analytical data that provide a good understanding of basalt-hosted systems. However, the discovery of the low-temperature, peridotite-hosted Lost City Hydrothermal Field (LCHF, Fig. 1; Kelley et al., 2001) in 2000 has highlighted an entirely different form of seafloor hydrothermal activity in a previously poorly explored off-axis setting and driven by serpentinization reactions and lithospheric cooling (Kelley et al., 2001; Früh-Green et al., 2003; Allen and Seyfried, 2004; Kelley et al., 2005; Ludwig et al., 2006). Serpentinized peridotites are relatively common at slow-spreading ridges (e.g., Cannat, 1993; Lagabrielle et al., 1998; Alt and Shanks, 2003; Früh-Green et al., 2004) and Lost City is unlikely to be unique. Studies of this system suggest that geochemical fluxes associated with serpentinization reactions are distinctly different than black smoker systems driven by magmatic activity (Kelley et al., 2005; Brazelton et al., 2006; Ludwig et al., 2006; Proskurowski et al., 2006).

During the last 20 years B-isotopes have increasingly been used as geochemical tracers in petrogenetic and ore deposit studies, and for modeling geochemical cycles in the Earth's mantle, crust and oceans (e.g., Spivack et al., 1987; Palmer and Slack, 1989; Ryan and Langmuir, 1993; Palmer, 1996; Lemarchand et al., 2000; Turner et al., 2007). In particular, after the discovery that arc magmas are variably enriched in B with respect to mid-ocean ridge magmas (Leeman, 1987; Morris et al., 1990), many studies have used B isotopes to unravel volatile transfer processes from the subducting oceanic crust to the mantle wedge and to arc magmatism (e.g., Palmer, 1991; Ishikawa and Tera, 1999; Rosner et al., 2003; Leeman et al., 2004; Savov et al., 2005a). Early studies suggested a central role of altered oceanic crust and sediments as sources of fluids and B (e.g., Ishikawa and Tera, 1999); however, more recent papers have emphasized the potential role of subducted serpentinites as an important source of B-rich fluids to supra-subduction systems (Straub and Layne, 2002; Savov et al., 2005a; Tonarini et al., 2007). In spite of an increasing interest in understanding serpentinites geochemistry, the B-isotope composition of oceanic serpentinites remains poorly documented (Spivack and Edmond, 1987; Simon et al., 2006). Isotopic data on this potentially important boron reservoir is crucial to properly model boron isotope systematics during metasomatic/magmatic processes in subduction zones and to estimate the global flux of boron isotope exchange with seawater in oceanic environments.

Here, we present a B-, O-, and Sr-isotope study of altered basement rocks sampled on the southern ridge of the Atlantis Massif oceanic core complex and in the vicinity of the Lost City Hydrothermal Field. These data are used to model the influence of pH, fluid temperature, and mineralogy on the B-isotope geochemistry during fluid–rock interactions at varying temperatures. The Atlantis Massif (AM) and the LCHF (Fig. 1) provide a natural laboratory for studying the tectonic and metamorphic evolution of an off-axis, ultramafic-hosted hydrothermal system that has been active for at least 30,000–40,000 years (Früh-Green et al., 2003; Kelley et al., 2005; Ludwig et al., 2006). Results from this study show a close link between tectonic processes, changes in fluid flow and changes in geochemical signatures of the fluids, and provide new constraints on fluid/rock interaction and mass transport during long-lived detachment faulting and exhumation of an oceanic core complex.

2. GEOLOGICAL SETTING AND FIELD STUDIES

The dome-like Atlantis Massif (Fig. 1) is located at 30°N at the intersection of the Mid-Atlantic Ridge (MAR) and the Atlantis Transform Fault (Cann et al., 1997; Blackman et al., 1998; Blackman et al., 2002; Karson et al., 2006). The central dome of the massif shows a distinct corrugated morphology, which is interpreted as the surface expression of a low-angle detachment fault that led to uplift and exposure of lower crustal and upper mantle sequences over the past 1.5–2 Myr (Cann et al., 1997; Blackman et al., 1998; Blackman et al., 2002). The top of the massif is covered by variably lithified pelagic carbonates and dispersed outcrops of sedimentary breccias (Schroeder et al., 2002; Früh-Green et al., 2003; Blackman et al., 2002; Karson et al., 2006). A prominent eastern ridge on the flank of the massif consists of basaltic lavas interpreted as an allochthonous, hanging-wall block atop the detachment fault (Blackman et al., 2002; Karson et al., 2006).

The domed morphology and exposure of variably altered and deformed gabbroic and ultramafic sequences during phases of asymmetric extension and detachment faulting are considered key components that define oceanic core complexes (OCCs). More recent investigations in the Atlantic by Smith et al. (2006) suggest that OCCs may be a common feature of slow-spreading ridges and emphasize the distinct differences in crustal architecture, magmatic activity, and accretion processes between fast- and slow-spreading ridges. The central dome of the AM was the target of two expeditions of the Integrated Ocean Drilling Program (IODP Site 1309, Expeditions 304 and 305; Blackman et al., 2006; Ildefonse et al., 2007) and recovered 1400 m of predominantly gabbroic rocks. The results of drilling highlighted the highly heterogeneous nature of magmatic crustal accretion, deformation, and alteration processes during formation of OCCs.

Normal faulting and mass-wasting along the southern ridge of the AM (Fig. 1) have resulted in a near-vertical, ~3800 m high, transform-parallel scarp that provides a window into the basement below Lost City (Kelley et al., 2005; Karson et al., 2006). The southern ridge of the AM and the LCHF were mapped and sampled during three cruises: AT3-60 (MARVEL expedition, 2000) and AT7-34 (2003) using the submersible Alvin with the R/V *Atlantis*; and in 2005 using the remotely operated vehicles (ROV) *Hercules* and *Argus* onboard the R/V *R.H. Brown*. Dive tracks, lithologies and sample locations are given in

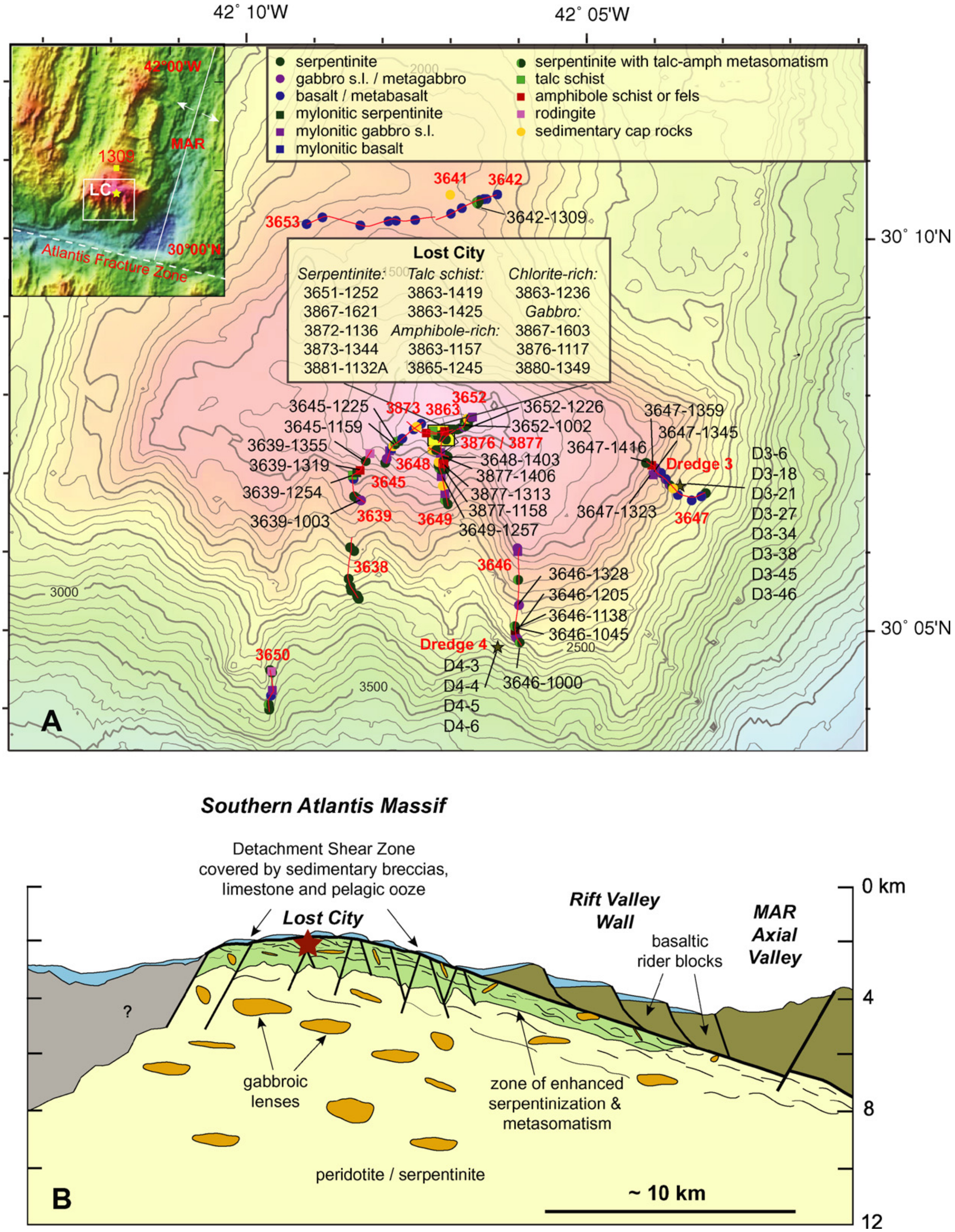

Fig. 1. (A) Bathymetric map of the southern Atlantis Massif (modified from Blackmann et al., 2002), showing Alvin dive tracks (in red), sample localities and lithologies of samples completed during the 2000 (dives 3639 through 3652) and 2003 cruises (dives 3862 through 3881). Dense locations of *Alvin* dives around the Lost City Hydrothermal Field (yellow shaded box) have been omitted for clarity. Inset shows local plate boundaries and location of the massif, Lost City (LC), and IODP Site 1309. White box in inset shows area of sampling. (B) Schematic east–west cross section of the southern Atlantis Massif (after Boschi et al., 2006a) showing gabbroic lenses embedded in peridotite and in the detachment fault as well as cross-cutting normal faults and a zone of metasomatism and enhanced serpentinization along the detachment fault (light green). Focusing of fluids along the detachment zone, in discrete shear zones, and along the normal faults resulted in pervasive alteration of the serpentinites and gabbros along the outer wall of the southern massif.

Fig. 1A. The southern ridge of the massif consists primarily of variably altered and deformed peridotites (~70% of total samples) that have been intruded by smaller bodies of gabbro, pyroxenite, and minor basalt, and are covered with a flat-lying, 1–2 m thick sedimentary sequence (Fig. 1B; Nooner et al., 2003; Blackman et al., 2002; Kelley et al., 2005; Sogalevich et al., 2005; Karson et al., 2006).

The peridotites are primarily depleted spinel harzburgites, consisting of olivine, orthopyroxene, and chromium spinel with minor clinopyroxene. The rocks are highly serpentinized (from 70% to 100%); primary olivine and orthopyroxene are replaced by serpentine and magnetite that form typical ribbon/mesh pseudomorphic serpentine textures, and minor (<5 vol%) chlorite, amphibole and talc. Brucite and Fe–Ni alloys, which are often minor constituents of oceanic serpentinites, were not found in any of the studied serpentinite samples. Multiple phases of serpentine growth and overprinting textures suggest that seawater penetration and serpentinization commenced close to the ridge axis and continued throughout the tectonic evolution of the massif.

The gabbroic rocks at the southern AM include variably altered and deformed medium- to coarse-grained gabbro, oxide gabbro, gabbronorite, pyroxenite, and microgabbro (Blackman et al., 2002; Schroeder and John, 2004; Boschi et al., 2006a). Primary minerals consist of plagioclase, clinopyroxene, oxide phases, and minor amounts of orthopyroxene. The secondary mineral assemblages and textures of the gabbroic rocks in particular record deformation and recrystallization under high-grade granulite to amphibolite facies conditions during the early phases of exhumation (Schroeder and John, 2004; Boschi et al., 2006a). These are overprinted by greenschist facies alteration and local rodingitization. The greenschist facies assemblages are dominated by actinolite, tremolite, and chlorite. Minor late alteration is marked by zeolite and prehnite veins that cut the higher temperature mineral assemblages and deformation fabrics. In comparison to the southern wall, the gabbroic rocks from IODP Hole 1309D at the central dome are less deformed and are dominated by secondary assemblages that reflect moderate temperature alteration (<500 °C). Alteration and deformation are generally restricted to the upper 800 m of the hole or to fault zones (Blackman et al., 2006). Talc metasomatism in the recovered drill core at the central dome is limited to a few talc-tremolite schists, to contacts between ultramafic and gabbroic rocks, and to corona formation between olivine and plagioclase in olivine-bearing gabbros (Blackman et al., 2006).

Field studies in 2003 provided detailed observations and samples of a well-defined, continuous, low-angle detachment shear zone (DSZ) at the top of the south wall of the AM (Fig. 1B; Karson et al., 2006). The shear zone is ~100 m thick and is marked by variably deformed, metasomatic talc- and/or amphibole-rich fault rocks, which record strain localization and evidence for focused fluid flow (Schroeder and John, 2004; Boschi et al., 2006a). Metasomatic alteration to form talc- and amphibole-rich rocks (Fig. 2) occurs locally throughout the southern wall but is a key aspect of the DSZ and is similar to alteration along detachment faults in other OCCs (Boschi et al., 2006b and references therein). Petrographic and geochemical data indicate that the protoliths of the talc-rich rocks are serpentinized peridotites, whereas the amphibole-rich rocks are dominated by protoliths of mafic composition (Boschi et al., 2006a).

The LCHF is located on a fault-bounded terrace near the top of the south wall of AM (Fig. 1) and consists of numerous, up to 60 m tall, carbonate–brucite structures that emit diffuse 40–90 °C, high-pH (9–11) fluids with low-Mg, metals, and silica concentrations (Kelley et al., 2001, 2005). Enrichments in Ca, H_2, and CH_4 and a near lack of CO_2 in the fluids (Kelley et al., 2005; Proskurowski et al., 2006) attest to ongoing serpentinization processes and cooling of lithospheric material at depth (Allen and Seyfried, 2004; Kelley et al., 2005; Ludwig et al., 2006). Hydrogen isotope data on H_2 and CH_4 in the vent fluids suggest present-day serpentinization temperatures in the basement that are approximately 20–60 °C higher than those measured at the Lost City vents (Proskurowski et al., 2006). The southern wall is cut by a series of steeply dipping, transform-related faults that control much of the focused flow throughout the field (Fig. 1B; Kelley et al., 2005; Karson et al., 2006). In addition, sub-horizontal foliations in the basement rocks provide permeable pathways for nearly horizontal sheet-like fluid flow, which locally produces hydrothermal mineral growths that reach up to 10 m in height (Kelley et al., 2005; Ludwig et al., 2006).

3. METHODS

3.1. Samples

This study is based on mineralogical, petrological, and geochemical investigations of >150 samples and is part of an extensive multidisciplinary project aimed at understanding the crustal architecture, alteration history and exhumation of the Atlantis Massif as an OCC and carried out in collaboration with the University of Washington and Syracuse University. The geology of the area and studies of the mineral assemblages, bulk rock geochemistry, and mass transfer associated with the formation of the detachment shear zone and metasomatic fault rocks are described in detail in Karson et al. (2006) and Boschi et al. (2006a). The geochemical study presented here primarily focuses on samples collected in 2000 but incorporates yet unpublished petrological, geochemical, and isotopic results produced by our group at the ETH Zurich on the entire sample set collected from the three cruises (e.g., Delacour et al., 2004, 2007; Früh-Green et al., 2007). A compilation of selected elements used in the discussion below is given in Table 1.

Bulk rock analyses of major and trace element compositions were carried out on 91 samples from the south wall of the Atlantis Massif, and O- and H-isotope compositions were determined on a subset of these. Ten representative serpentinized rocks and six fault rocks were then chosen for further B- and Sr-isotope analyses (Table 2). The samples selected for B and Sr isotope analyses were free of late fractures, carbonate veins, and reddish oxidization haloes; these also contained less than 0.62 wt% CO_2 with most of

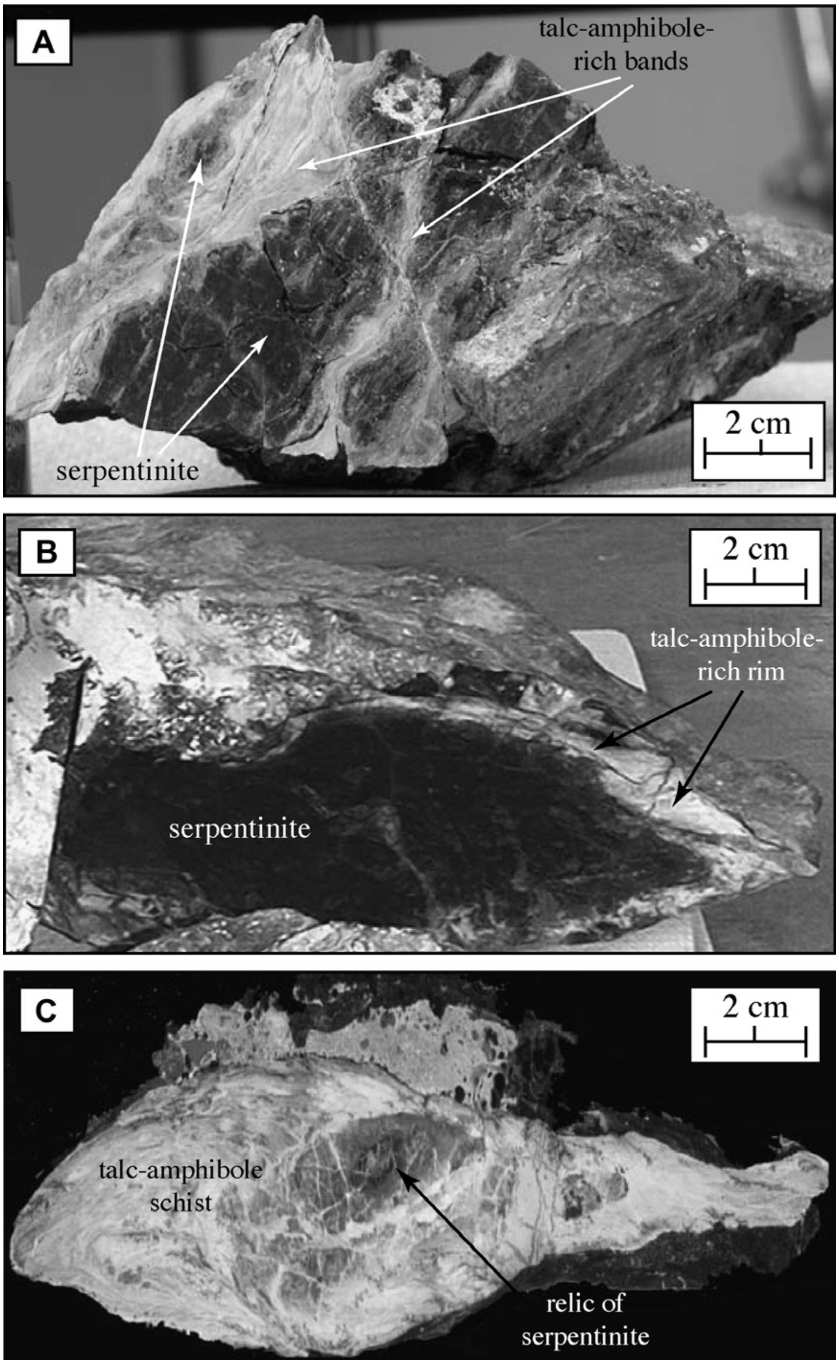

Fig. 2. Representative examples of fault rocks: (A) 3873-1124 and (B) 3639-1254 metasomatic talc–amphibole-rich bands (light colored domains) postdate serpentinite mineral assemblage (dark domains); (C) 3645-1225 typical talc–amphibole schist showing heterogeneous high strain crystal–plastic textures. The synkinematic talc–amphibole assemblages wrap around strongly deformed relicts of serpentinite (dark domains).

the samples below 0.09 wt% (Table 1). To avoid chemical signatures from late-stage weathering, the external rims of the samples were systematically removed.

Samples 3639-1254 and 3645-1159 are representative examples of deformed serpentinites that were progressively affected by localized Si- (talc)metasomatism (Fig. 2). They consist of lenses of serpentinite (serpentinized cores = C) enclosed by mm-sized whitish, sheared domains consisting of metasomatic talc- and amphibole-rich assemblages (rim = R). The lens-shaped central domains characteristically exhibit a lower degree of serpentinization and contain enclaves of primary olivine. These relationships indicated that local domains of olivine were relatively stable during detachment faulting. Samples 3639-1254 and 3645-1159 were cut into two portions and analyzed separately to evaluate small-scale geochemical and isotopic exchange during

Table 1
Geochemical, oxygen, and hydrogen isotope data of the Atlantis Massif serpentinites, fault rocks, and gabbros

Sample	Type	Depth (m)	Latitude, N	Longitude, W	SiO_2 (wt%)	MgO (wt%)	CaO (wt%)	LOI (wt%)	CO_2 (wt%)	Sr (ppm)	B (ppm)	$\delta^{18}O$ (‰)	δD (‰)
3639-1355	Serpentinite	1295	30°7.153′	42°8.226′	38.58	38.86	0.15	13.71	0.06	7	90.4	4.7	
3647-1416	Serpentinite	1555	30°7.130′	42°4.132′	38.53	39.12	0.05	12.98	0.04	4	61.9	4.5	
3648-1403	Serpentinite	1067	30°7.233′	42°7.062′	40.22	37.81	0.03	12.73	<0.01	6	34.0	5.6	
3651-1252	Serpentinite	792	30°7.407′	42°6.968′	37.64	40.01	0.04	13.55	0.03	3	71.6	3.2	−62
3652-1226	Serpentinite	805	30°7.603′	42°6.759′	38.35	39.64	0.14	13.05	0.09	4	90.6	6.7	
D3-6	Serpentinite	2150	30°6.844′	42°3.702′	39.03	37.61	0.12	12.82	0.14	3		4.1	
D3-18	Serpentinite	2150	30°6.844′	42°3.702′	38.28	36.89	0.03	12.34	0.05	6		3.0	
D3-27	Serpentinite	2150	30°6.844′	42°3.702′	38.41	39.63	0.03	12.42	0.03	<2	65.2	3.0	
D3-34	Serpentinite	2150	30° 6.844′	42°3.702′	37.84	39.99	0.07	13.29	0.05	4	63.4	3.5	
3867-1621	Serpentinite	759	30°7.482′	42°7.140′	38.17	38.29	0.08	13.70	0.03	4	77.0		
3872-1136	Serpentinite	798	30°7.482′	42°7.134′	38.59	37.49	0.17	13.51	0.03	4		4.5	
3877-1158	Serpentinite	1115	30°7.026′	42°7.122′	38.59	38.40	<0.01	13.33	0.04	3		3.3	−69
3877-1344	Serpentinite	913	30°7.320′	42°7.206′	37.95	38.23	<0.01	13.77	0.02	3		4.3	
3877-1406	Serpentinite	908	30°7.320′	42°7.200′	37.37	39.82	0.1	13.63	0.07	5	63.4	2.7	−72
3881-1132A	Serpentinite	822	30°7.422′	42°7.098′	38.34	38.18	0.16	13.88	0.07	6	48.5	4.1	−63
3646-1000	Serpentinite + metasomatism	2507	30° 4.874′	42°6.002′	49.87	29.53	2.94	6.91	0.01	5		3.8	
3873-1344	Serpentinite + metasomatism	923	30°7.332′	42°7.686′	37.95	38.23	<0.01	13.77	0.02	3	64.8	3.2	−86
D4-3s	Serpentinite rim	2730	30°4.874′	42 6.319′	39.16	36.34	0.48	11.99	0.07	5	57.4	2.0	−62
D4-3m	Mylonitic olivine-rich core	2730	30°4.874′	42°6.319′	43.59	35.81	2.62	6.55	0.14	21	14.3	3.8	−55
3639-1254C	Serpentinite core	1474	30°6.955′	42°8.406′	39.26	36.47	1.60	11.64	0.29	15	73.9	3.3	−61
3645-1159C	Serpentinite core	957	30°7.355′	42°7.826′	49.47	32.88	1.60	9.16	0.62	25	38.2	2.6	−71
3639-1254R	Metasomatic rim	1474	30°6.955′	42°8.406′	42.87	30.66	4.92	9.37	0.23	33	28.7	1.7	−92
3645-1159R	Metasomatic rim	957	30°7.355′	42°7.826′	56.80	28.89	4.52	5.68	0.02	3	16.6	2.9	−63
3642-1309	Tal-rich fault rock	1751	30° 10.297′	42°6.990′	53.11	26.81	2.60	5.51	0.02	5	14.4	3.5	
3645-1225	Tal-rich fault rock	955	30°7.354′	42°7.819′	53.84	28.57	6.09	6.92	0.19	7	38.6		
D3-46	Tal-rich fault rock	2150	30°6.844′	42°3.702′	49.69	31.34	0.92	6.17	0.03	<2	<0.2	2.1	
D4-4	Tal-rich fault rock	2730	30°4.874′	42°6.319′	58.87	27.90	0.12	5.26	0.01	<2	3.2	3.1	
3863-1419	Tal-rich fault rock	794	30°7.542′	42°7.356′	53.96	26.70	8.06	4.94	0.01	6		4.4	−62
3863-1425	Tal-rich fault rock	794	30°7.542′	42°7.356′	46.63	32.17	3.55	9.24	0.01	5		2.8	
3873-1124	Tal-rich fault rock	959	30°7.416′	42°7.842′	52.95	27.85	7.15	6.13	0.14	7		2.0	−102
3639-1319	Amphibole-rich fault rock	1416	30°7.028′	42°8.321′	42.85	21.77	7.33	5.48	0.01	6		2.3	
3646-1205	Amphibole-rich fault rock	2327	30°4.929′	42°6.029′	49.69	24 22	6.24	4.59	0.01	5	3.0		
3647-1359	Amphibole-rich fault rock	1623	30°6.996′	42°4.050′	50.84	26.48	2.68	5.29	<0.01	5	4.1	4.1	
D3-21	Amphibole-rich fault rock	2150	30°6.844′	42°3.702′	49.30	27.21	2.65	5.85	0.03	6	2.3		
D3-45	Amphibole-rich fault rock	2150	30°6.844′	42°3.702′	43.87	21.80	4.55	5.45	0.21	4	3.0		
3863-1157	Amphibole-rich fault rock	862	30°7.506′	42°7.410′	51.30	21.99	11.64	2.15	0.02	7	1.6		
3865-1245	Amphibole-rich fault rock	795	30°7.452′	42°7.218′	49.41	22.20	10.31	3.72	0.01	8	<0.2		
3877-1313	Amphibole-rich fault rock	1009	30°7.224′	42°7.140′	54.95	23.34	12.30	2.98	0.31	7		2.0	−45
3863-1236	Chlorite-rich fault rock	837	30°7.512′	42°7.416′	28.22	31.26	0.11	12.32	0.02	4		3.7	
3639-1003	Gabbro	1648	30°6.600	42°8.350′	51.74	9.21	10.88	0.19	<0.01	97	1.9		
3646-1045	Gabbro	2466	30°4.873′	42°5.978′	52.16	7.35	12.29	0.69	0.03	103		4.9	

3646-1138	Gabbro	2393	30°04.85	42°6.000′	49.76	8.56	12.05	0.76	<0.01	66	4.9		
3646-1328	Gabbro	2043	30°5.336′	42°5.997′	46.63	12.08	6.96	4.53	0.54	80	3.6		
3647-1345	Gabbro	1661	30°7.091′	42°4.051′	55.19	7.96	9.63	0.66	0.01	115	<0.2		
3649-1257	Gabbro	1188	30°6.969′	42°7.135′	50.32	8.79	11.92	0.45	0.02	112	3.7		
D4-6	Gabbro	2730	30°4.874′	42°6.319′	48.64	8.16	11.81	1.69	0.58	143	10.7		
D4-5	Gabbro	2730	30°4.874′	42°6.319′	46.88	21.12	8.83	3.46	0.07	17	<0.2		
3647-1323	Gabbro	1755	30°7.007′	42°3.921′	46.63	9.10	8.02	1.42	0.02	77	2.1		
3867-1254	Myl. Gabbro	843	30°7.356′	42°7.200′	47.90	11.39	11.30	4.38	0.01	137		3.7	−100
3867-1603	Gabbro	748	30°7.488′	42°7.134′	49.69	10.52	10.26	2.63	<0.01	139		3.0	−54
3876-1117	Gabbro	869	30°7.458′	42°7.122′	52.36	9.81	11.29	1.42	<0.01	119		2.8	
3880-1349	Oxide gabbro	819	30°7.236′	42°7.086′	33.09	8.95	11.54	2.57	<0.01	50		4.2	−69
3652-1002	Gabbro + metasomatism	732	30°7.459′	42°7.146′	36.70	24.48	2.52	12.10	0.03	39	26.1		
D3-38	Fe–Ti-rich Gb + metasomatism	2150	30°6.844′	42°3.702′	32.11	15.77	6.91	6.30	0.02	49	<0.2		

transformation from serpentinite to talc schist during detachment faulting (Fig. 2 and Table 1).

3.2. Analytical procedures

Bulk rock major and trace element analyses (Figs. 3 and 4) were performed by inductively coupled plasma-mass spectrometry (ICP-MS); a preliminary subset was measured at CRPG-Nancy (France) and the remainder were measured at the Activation Laboratories Ltd. (Ancaster, Canada). Duplicate analyses of control samples were conducted at the two laboratories to guarantee analytical consistency and results are within 2% or less for all elements. Determination of total inorganic carbon contents (TIC), released as CO_2 from carbonate phases, was carried out at the Geological Institute, ETH Zurich by coulometric titration (Coulometer UIC CM5012). CO_2 was liberated and analyzed by reaction of HCl with 20–30 mg of bulk rock powder in glass capsules. Analytical precision of the instrument is ±0.1 wt%; relative analytical reproducibility of repeat measurements of standard carbonate was ±2%. Loss on ignition (LOI) was determined by weight difference following ignition of samples in a furnace, and since CO_2 contents are low, the LOI primarily reflects the water contents in the rocks.

Boron concentrations were determined at Activation Laboratories Ltd. (Ancaster, Canada). One gram of sample powders was encapsulated in a polyethylene vial and placed in a thermalized beam of neutrons produced from a nuclear reactor. Samples were measured for the doppler broadened prompt gamma ray at 478 keV using a high purity Ge detector. Samples were compared to certified reference materials used to calibrate the system (detection limit is 0.2 ppm).

Boron isotope compositions were determined using a VG Isomass 54E positive thermal ionization mass spectrometer (at IGG-CNR, Pisa), following separation of boron by ion-exchange procedures as described by Tonarini et al. (1997). Total procedure blanks were 10 ng and are negligible relative to the amount of sample processed. Procedure accuracy was evaluated by repeated analyses of the NIST SRM 951 standard taken through the full chemistry steps and through replicate analysis of GSJ-JB2 basalt reference standard (Tonarini et al., 1997). GSJ-JB2 yielded an average $\delta^{11}B = 7.01 \pm 0.10‰$ ($2\sigma_{mean}$). Isotopic fractionation associated with the mass spectrometer analysis was eliminated using a fractionation factor, calculated as $(R_{cert} + 0.00079)/R_{meas}$, for NIST SRM 951 ($^{11}B/^{10}B_{meas} = 4.0529 \pm 0.0007$). Boron isotope compositions are reported in the conventional delta notation ($\delta^{11}B$) as per mil (‰) deviation from the accepted composition of NIST SRM 951 (certified $^{11}B/^{10}B = 4.04362$; Catanzaro et al., 1970). The reproducibility of isotopically homogeneous samples treated with alkaline fusion chemistry is 0.5‰ (Tonarini et al., 1997, 2003), and replicate analyses of samples agree within this limit.

Sr isotope analyses were performed using a Finnigan MAT 262V multicollector mass-spectrometer (at IGG-CNR, Pisa) after conventional ion-exchange procedures for Sr separation; Sr total blank was better than 2 ng during

Table 2
Boron and strontium isotope compositions of the Atlantis Massif serpentinites and fault rocks

Sample	Rock type	B (ppm)	$^{11}B/^{10}B$	2σ	$\delta^{11}B$	2σ	$^{87}Sr/^{86}Sr$	2σ
3639-1355	Serpentinite	90.4	4.1049	0.0009	15.15	0.22	0.709087	0.000021
3648-1403	Serpentinite	34.0	4.0906	0.0022	11.62	0.54	0.709100	0.000016
3652-1226	Serpentinite	90.6	4.1030	0.0013	14.68	0.32	0.709056	0.000011
3651-1252	Serpentinite	71.6	4.1024	0.0019	14.53	0.46	0.708915	0.000013
3881-1132A	Serpentinite	48.5	4.0924	0.0014	12.07	0.34	0.709112	0.000015
3873-1344	Serpentinite	64.8	4.0987	0.0011	13.62	0.27	0.709088	0.000012
D4-3S	Serpentinite	57.4	4.0914	0.0012	11.82	0.29	0.709171	0.000013
D4-3M	Serpentinite	14.3	4.0896	0.0016	11.38	0.39	0.709024	0.000011
3639-1254 R	Metasomatic rim	28.7	4.0945	0.0018	10.27	0.44	0.707907	0.000014
3639-1254 C	Serpentinitic core	73.9	4.1186	0.0016	16.21	0.39	0.709093	0.000018
3645-1159 R	Metasomatic rim	16.6	4.0918	0.0024	9.60	0.59	0.707347	0.000016
3645-1159 C	Serpentinitic core	38.2	4.1063	0.0009	13.17	0.22	0.709064	0.000012
3642-1309	Talc schist	14.4	4.0911	0.0018	9.43	0.44	0.708467	0.000011
D4-4	Talc fels	3.2	4.0890	0.0017	8.91	0.42	0.708113	0.000013
3646-1205	Amph schist	3.0	4.0941	0.0016	10.17	0.39	0.704322	0.000014
3647-1359	Amph schist	4.1	4.0885	0.0016	8.78	0.39	0.705417	0.000012

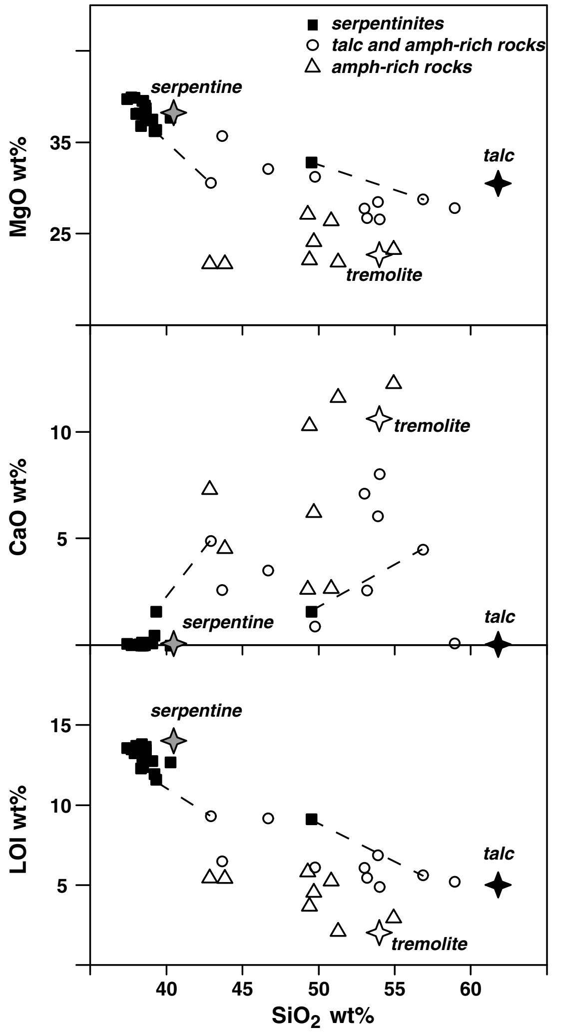

Fig. 3. Representative major element diagrams showing the relationships between geochemistry and mineralogy of the studied rocks; the composition of serpentine, talc, and tremolite are also reported. Serpentinite relic cores and metasomatic rims for samples 3645-1159 and 3639-1254 are connected by dashed lines.

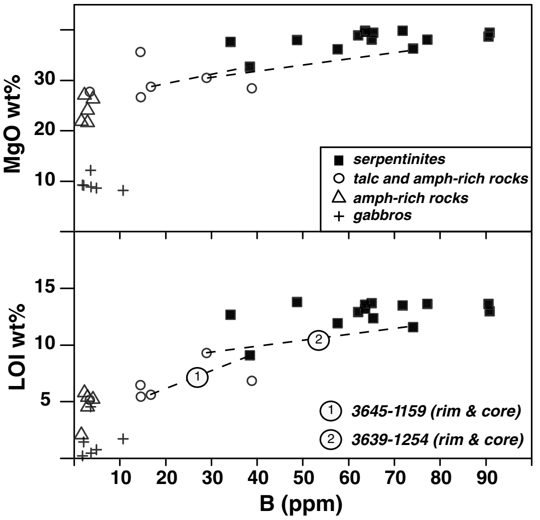

Fig. 4. Boron content versus loss of ignition (LOI) and MgO. Full squares are serpentinites, open circles are talc–amphibole-rich fault rocks (serpentinite protoliths), and open triangles are amphibole-rich fault rocks (mafic protoliths). Some slightly altered gabbro samples are reported as crosses. Core–rim, serpentinites–metasomatic samples are connected by dashed lines.

the period of measurements. Measured $^{87}Sr/^{86}Sr$ ratios have been normalized to $^{86}Sr/^{88}Sr = 0.1194$. During the collection of isotopic data, 12 replicate analysis of SRM 987 ($SrCO_3$) standard gave an average value of 0.710200 ± 8 (2σ mean). All $^{87}Sr/^{86}Sr$ data were normalized to a value of 0.71025 for the SRM 987 standard.

Oxygen isotope compositions were determined on CO_2 from decarbonated bulk rock powders at the ETH Zurich and the Scottish Universities Environmental Research Centre (SUERC) and are reported as $\delta^{18}O$ values in permil (‰), relative to Vienna Standard Mean Ocean Water (V-SMOW). At the ETH Zurich, oxygen was liberated by conventional fluorination reaction with ClF_3 in vacuum in nickel vessels overnight at 650 °C. Prior to fluorination and reaction, the bulk powders were heated under vacuum at 200 °C for a minimum of 2 h to remove interlayer and adsorbed surface water. $\delta^{18}O$ of samples measured at SUERC was determined by laser fluorination techniques following the Macaulay et al. (2000) modification of Sharp (1990). Samples were heated to 120 °C overnight under high vacuum prior to fluorination. To extract oxygen, ~1 mg was reacted with ClF_3 whilst heated with a CO_2 laser. At both laboratories, the resultant oxygen was purified, converted to CO_2 with heated graphite and the yield measured by capacitance manometer. The oxygen isotopic composition of the CO_2 was measured by a dual-inlet mass spectrometer with a working standard gas calibrated against international reference materials. The precision and accuracy of the measurements at both laboratories are ±0.2‰ (1σ) and NBS 28 gives 9.6‰. Hydrogen isotope compositions (δD ‰ V-SMOW) were determined at SUERC using the method described by Fallick et al. (1993) and using a chromium reduction furnace to convert released H_2O to H_2. The precision of δD is approximately ±3‰ (1σ), reproducibility of individual AM samples was ±6‰, and NBS30 was $\delta D = -65$‰.

4. RESULTS

Boron uptake in oceanic rocks occurs by two main mechanisms: (1) direct incorporation of boron during crystallization of structurally favorable, "B-rich" hydrothermal-diagenetic minerals (e.g., phyllosilicates; Spivack et al., 1987; Williams et al., 2001); and (2) adsorption from (sea)water by clays, other phyllosilicates and other secondary minerals during low-temperature interaction of fluids with sedimentary, crustal, and mantle rocks (Schwarcz et al., 1969; You et al., 1996). Although some authors suggest that the highest boron contents in serpentinites are related to low-temperature exchange (Bonatti et al., 1984), others provide boron isotope evidence for boron incorporation at higher temperature (Spivack and Edmond, 1987; Palmer, 1996). Below we present isotopic and geochemical data that indicates boron uptake during relatively high-temperature serpentinization (150–250 °C) at the Atlantis Massif. Samples with similar degrees of serpentinization have variable boron concentrations (Fig. 4), and we argue that other factors, such as pH and fluid fluxes, likely affect the uptake of boron and determine final boron isotope compositions of oceanic serpentinites.

4.1. Bulk rock geochemistry and boron content

The serpentinized spinel harzburgites recovered along the south wall of the AM have relatively homogeneous major element contents (Fig. 3) that are similar to those observed in the most depleted peridotites sampled in oceanic settings and ophiolite massifs (e.g., Niu, 2004; Paulick et al., 2006). The talc- and amphibole-rich rocks are characterized by higher SiO_2 and CaO contents, and lower MgO and water contents compared to the AM serpentinites. The bulk rock compositions of the serpentinites, talc, and amphibole fault rocks largely reflect the differences in mineralogy and the relative modal proportions of the main alteration minerals serpentine, talc, and tremolite acquired during serpentinization and Si-metasomatism.

Boron concentrations of the serpentinites, fault rocks, and gabbros from the southern wall (Table 2) are shown versus MgO and LOI content in Fig. 4. Boron is consistently highest in the serpentinites (34–91 ppm), and concentrations in the talc-rich rocks are <39 ppm. The lowest B concentrations are found in the amphibole-rich metasomatic rocks and the gabbroic rocks (2–4 ppm). The B content of the depleted mantle is estimated to be 0.06 ppm (Salters and Stracke, 2004); therefore, serpentinization processes at the AM clearly produced a 3 orders of magnitude increase in boron. This estimate is in agreement with reported boron data on serpentinites by other authors (e.g., Thompson and Melson, 1970; Bonatti et al., 1984; Spivack and Edmond, 1987; Früh-Green et al., 2004; Savov et al., 2005a,b). Our data clearly show that in contrast to strong B enrichment during serpentinization, talc metasomatism at the AM is associated with pronounced B depletion (Fig. 4).

4.2. Isotopic compositions

The boron isotope compositions of the Atlantis Massif basement rocks range from 8.8‰ to 16.2‰ (Table 2 and Fig. 5) and are distinctly lower than the seawater value of 39.5‰ (Spivack and Edmond, 1987). The serpentinite samples are enriched in ^{11}B ($11.4‰ < \delta^{11}B < 16.2‰$) with respect to the talc- and amphibole-rich fault rocks, which form the lighter end of the range ($8.8‰ < \delta^{11}B < 10.3‰$). The $\delta^{11}B$ values are positively correlated with B content but show no clear relationships with $\delta^{18}O$ or $^{87}Sr/^{86}Sr$ (Figs. 6 and 7). The two rim–core samples (3645-1159R/C and 3639-1254R/C) show a coherent behavior: the talc–amphibole rims have lower $\delta^{11}B$ values and B contents than the respective serpentinite relic cores (Fig. 5).

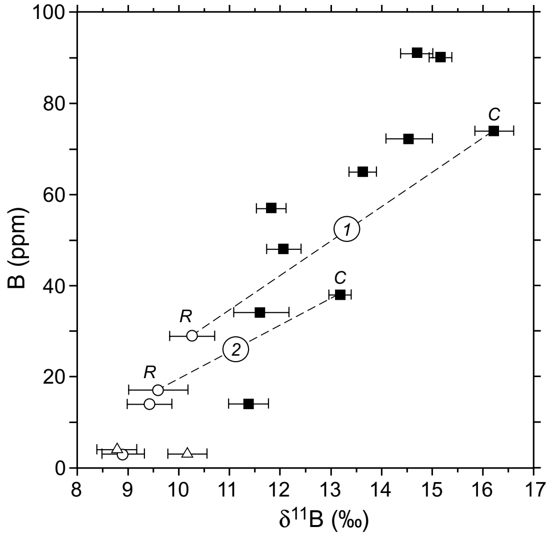

Fig. 5. Boron content versus $\delta^{11}B$ of rock samples from the southern wall of the Atlantis Massif. Full squares are serpentinites, open circles are talc–amphibole-rich fault rocks (serpentinite protoliths), and open triangles are amphibole-rich fault rocks (mafic protoliths). Core–rim, serpentinites–metasomatic samples are connected by dashed lines.

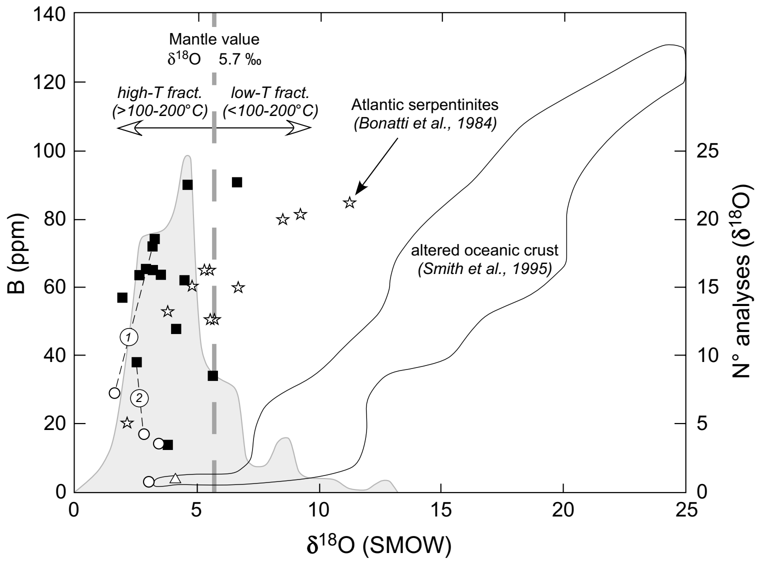

Fig. 6. Boron content versus δ^{18}O of rock samples from the Atlantis Massif compared with serpentinites from Bonatti et al. (1984) and altered basalts and gabbros from Smith et al. (1995). Symbols as in Fig. 3; errors for δ^{18}O are within the size of the symbols. The shaded area represents published δ^{18}O data in serpentinites compiled by Mével (2003), with the number of analyses shown on the right axis. The compilation of Mével (2003) shows a peak at 3–5‰ and a large dispersion between 0‰ and +12‰ indicative of a wide range of temperatures in ocean-floor serpentinites (see also Früh-Green et al., 2004). The AM serpentinites, in spite of the strongly variable B content show δ^{18}O values lower than unaltered mantle compositions and reflect moderately high-temperatures (>150–250 °C) over the integrated history of alteration. The talc- and amphibole-rich rocks have similar O-isotope compositions but systematically lower B contents.

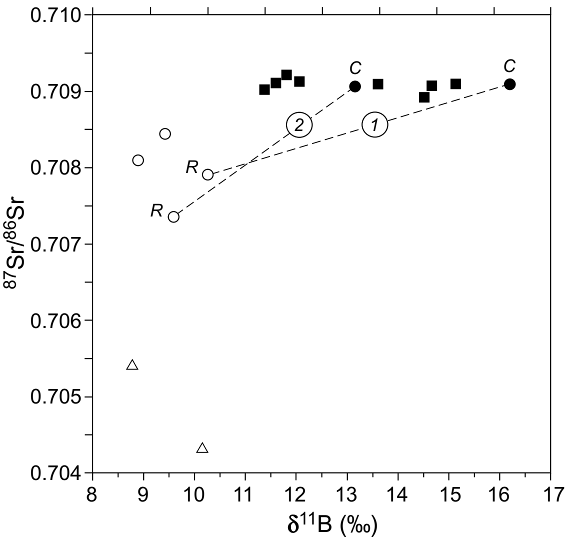

Fig. 7. ^{87}Sr/^{86}Sr versus δ^{11}B of rock samples from the Atlantis Massif. Full squares are serpentinites, open circles are talc–amphibole-rich fault rocks (serpentinite protoliths), and open triangles are amphibole-rich fault rocks (mafic protoliths). Core–rim, serpentinites–metasomatic samples are connected by dashed lines.

The bulk rock δ^{18}O and δD values of the serpentinites and talc–amphibole fault samples are characteristically low, ranging from 1.7‰ to 6.5‰ and −92‰ to −62‰, respectively (Table 1). The values lie within the known range of compositions of oceanic serpentinites (e.g., Wenner and Taylor, 1973; Sheppard, 1980; Sakai et al., 1990; Früh-Green et al., 1996; Mével, 2003; Früh-Green et al., 2004). Excluding one sample, the δ^{18}O data plot between MORB/mantle (∼5.7‰, Muehlenbachs, 1987) and seawater values (∼0‰) indicating a relatively high-temperature of fluid–rock interaction and variable fluid/rock ratios (Wenner and Taylor, 1973; Sheppard, 1980; Sakai et al., 1990; Früh-Green et al., 2004).

The δ^{18}O values show no significant correlation with B content and δ^{11}B (Fig. 6). The study of Bonatti et al. (1984) showed that both measured and corrected (normalized to volume percent serpentine) boron contents display a positive covariance with δ^{18}O. The AM peridotites have consistently high to very high degrees of serpentinization and show relatively constant LOI value (Fig. 4), thus, normalization to the degree of serpentinization would not change the observed random distribution.

The Sr isotope compositions of the AM basement rocks vary between mantle values and present-day seawater compositions (0.7043–0.7091; Table 2 and Fig. 7). The serpentinites define a narrow range of ^{87}Sr/^{86}Sr between 0.7089 and 0.7091, which reflects interaction with a seawater-dominated fluid and overlaps with the peak in distribution of published serpentinites ^{87}Sr/^{86}Sr ratios (e.g., Mével, 2003). In contrast to the serpentinites, the ^{87}Sr/^{86}Sr ratios of the talc- and amphibole-rich fault rocks consistently show lower values, ranging from 0.7073 to 0.7085 and from 0.7043 to 0.7054, respectively, and are closer to unaltered lower crustal and upper mantle compositions (Table 2 and Fig. 7).

The ^{87}Sr/^{86}Sr values of carbonate veins and fissures within the serpentinite basement of the Lost City hydrothermal field are distinctly lower (around 0.708 and Sr ∼2300 ppm; Ludwig et al., 2006) than the Sr isotope

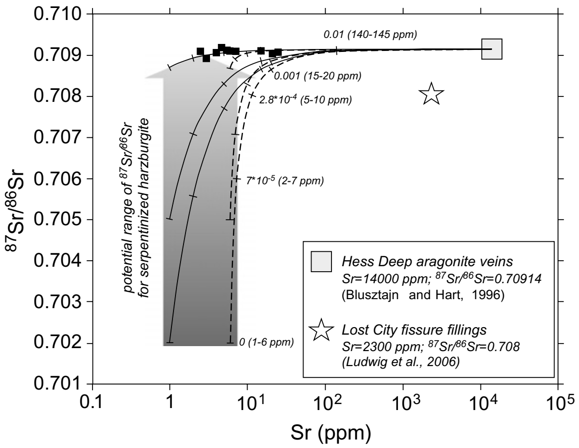

Fig. 8. Strontium content versus ^{87}Sr/^{86}Sr diagram showing mixing curves calculated for a hypothetical carbonate input into serpentinite. Full and dashed curves were calculated for an initial Sr content in serpentinites of 1 and 6 ppm, respectively. Numbers near the curves indicate the calculated fraction of carbonate component with strontium content in brackets.

compositions of the serpentinites (Fig. 8). This suggests that there has been negligible addition of Sr derived from hydrothermal carbonate, and thus there is an insignificant contribution of carbonate to the bulk rock Sr isotope signatures of the analyzed serpentinites, which is consistent with no apparent increase in Ca and the very low carbonate content of most samples ($CO_2 < 0.09$ wt%; Table 1). The very low Sr and CO_2 contents and the high ^{87}Sr/^{86}Sr values of AM serpentinites also exclude a possible carbonate reservoir in isotopic equilibrium with seawater. Fig. 8 shows mixing curves calculated for the addition of a carbonate component (Sr = 14,000 ppm, ^{87}Sr/^{86}Sr = 0.70914; Bonatti et al., 1980; Blusztajn et al., 1996) to a hypothetical "undisturbed" serpentinite with varying initial Sr contents and isotopic compositions (Sr = 1–6 ppm, ^{87}Sr/^{86}Sr = 0.702–0.705) and clearly shows that addition of carbonate cannot explain the Sr isotope compositions of the AM serpentinites. The curves overlap the measured dataset only for mixing with a serpentinite ^{87}Sr/^{86}Sr composition of 0.7087. Thus, even in the case of a slight carbonate contamination, we consider the high ^{87}Sr/^{86}Sr values measured in the AM basement to be signatures of Sr isotope exchange attained during the hydration of mantle rocks.

5. DISCUSSION

Boron isotope fractionation is controlled by changes in pH, temperature, and by physical and chemical properties of the constituent mineral phases. Thus, the interpretation of boron isotope data must take into consideration these complexities in isotopic behavior during fluid–rock interaction.

As in other studies of oceanic serpentinites, the mineral assemblages, and geochemical signatures of the AM serpentinites are the result of progressive serpentinization during a long-lived history of seawater infiltration, alteration and emplacement of the Atlantis Massif. Thus, the isotopic signatures of the rocks must be considered as an integrated signal of this history and will be influenced by reservoir type and sizes and degree of mass transfer during multiple episodes or continuous alteration.

5.1. Temperature constraints on alteration

A crucial parameter that must be addressed in understanding the boron geochemistry of the Atlantis Massif is the temperature of alteration. In addition, we must consider the question of whether the boron contents and isotopic compositions are signatures of hydrothermal/metasomatic processes or whether these compositions solely reflect chemical modifications and overprinting during subsequent interaction with seawater at very low temperature (i.e., seafloor weathering < ~25 °C) after exhumation and serpentinization of the peridotites.

The serpentinized peridotites collected along the southern wall of the AM show at least three stages of hydration characterized by an early stage of serpentinization and local veining that is overprinted by several distinct stages of serpentine formation. These are locally cut by veins filled with serpentine, talc, tremolite, or chlorite, but these veins represent a low percentage of the total modal mineralogy. Late-stage carbonate veins locally crosscut all earlier textures and alteration assemblages; however, for this study we excluded all samples with discrete veins and selected samples with very low CO_2 content (Table 1) to avoid any significant carbonate contamination. In some samples, the oxygen isotope compositions of the carbonate veins and carbonate in mesh cores record temperatures up to ~220 °C (Früh-Green et al., 2003; Kelley et al., 2005). Mg-rich clay minerals (e.g., smectites, sepiolite, and palygorskite), which usually mark low-temperature overprinting and seafloor weathering (Bonatti et al., 1983; Karpoff et al., 1989; Früh-Green et al., 2004), were not found in our samples.

The serpentinites show increasing B concentrations that correlate with increasing δ^{11}B values (Fig. 5) but show no correlation with δ^{18}O values. A positive correlation in B content and δ^{18}O, and a weak positive correlation of these with δ^{11}B, has been measured and modeled in studies of the upper oceanic crust (Spivack and Edmond, 1987; Smith et al., 1995; Simon et al., 2006). These studies show that the greatest B enrichments, the highest δ^{18}O, and in some cases, the lowest δ^{11}B values occur in the upper 500 m of the basaltic crust and ascribe such patterns to aging and prolonged low-temperature weathering close to the seafloor. In contrast to studies of the upper basaltic crust, the AM serpentinites have variable B contents (14–91 ppm) and a relatively narrow range of δ^{18}O values that are distinctly lower than unaltered mantle compositions of ~5.7‰ and provide constraints of temperatures of alteration (Table 1 and Fig. 6). The talc- and amphibole-rich rocks have similar oxygen isotope compositions, but their B contents are systematically lower than the serpentinites (Fig. 6).

Because serpentinization likely takes place over a range of temperatures during emplacement on the seafloor, temperature estimates based on bulk rock oxygen isotope data may be ambiguous. However, serpentine is the main alteration phase in the AM serpentinites and point-counting of 17 samples indicates that it constitutes approximately 60–80 modal percent of the samples. Accordingly, as shown in Fig. 3, the bulk rock geochemistry of the selected samples is almost entirely controlled by serpentine minerals. Thus, the bulk isotopic compositions of the serpentinites reflect the high modal percentage of serpentine and will be similar to analyses on bulk serpentine separates.

An integrated temperature of alteration can therefore be estimated by oxygen isotope serpentine–water fractionation factors (e.g., Taylor, 1977). Using the empirical serpentine–H_2O fractionation factors of Wenner and Taylor (1973) as modified by Früh-Green et al. (1996) and the open system model of Sakai et al. (1990), we calculate integrated temperatures of ~130 to 230 °C and variable water–rock ratios (W/R). Somewhat lower temperatures of 110–150 °C were calculated for the present-day thermal regime at Lost City from CH_4–H_2 hydrogen isotope data of the vent fluids (Proskurowski et al., 2006). These temperature estimates are in agreement with thermodynamic modeling of Allen and Seyfried (2004), which predicts that serpentinization at Lost City occurs at temperature of 200 ±50 °C.

5.2. Control of pH on B-uptake and -isotope compositions

Interpretation of boron isotope data in hydrothermally altered rocks requires the knowledge of a number of physical and chemical parameters. For example, pH and p*K* as well as the ionic strength of the hydrothermal solution can influence the modality and the extent of boron isotope fractionation between fluids and newly formed minerals (see Appendix A). In submarine hydrothermal systems the initial fluid is primarily seawater and represents an end-member with homogeneous boron content of 4.5 ppm and an isotopic composition of +39.5‰ that will be modified by water–rock reactions along its path through the oceanic lithosphere.

5.2.1. *B-uptake at low-temperature*

In Fig. 9, the speciation of boron and the relationships between the boron isotope composition of boron species and seawater pH have been calculated for ambient conditions of 0, 10, and 25 °C and are plotted together with the variation fields of serpentinites and weathered oceanic basalts (see Appendix A for calculation details). In the pH range of seawater, 85–95% of dissolved boron is trigonally coordinated as $B(OH)_3$ (Fig. 9a), while the rest is tetrahedrally coordinated as $B(OH)_4^-$. At low-temperature, boron adsorbed on the surfaces of clay minerals is in tetrahedral coordination, causing a large fractionation in the trigonal species in solution (Palmer et al., 1987). Fig. 9b clearly shows that the range of B-isotope compositions in most basalts reflect B-uptake at ambient seawater conditions. In contrast, the AM serpentinite compositions plot above the equilibrium curves and must indicate incorporation of B at higher temperatures.

The lack of correlation between B contents and $\delta^{18}O$, and thus calculated temperature, contrasts with the study of Bonatti et al. (1984), which documents a positive correlation between B and O-isotope compositions in serpentinite samples dredged along the MAR (Fig. 6). In spite of large uncertainties in temperature estimates using bulk rock $\delta^{18}O$ data, Bonatti et al. (1984) concluded that uptake of B is favored at low-temperatures (<50 °C). Low-temperature B uptake is also consistent with experiments of seawater–peridotite interaction of Seyfried and Dibble (1980), which showed that B concentrations in the fluids drastically decrease during very rapid cooling to 25 °C. In contrast, high B contents were found in serpentinites formed at greenschist-facies conditions from a number of ODP drill cores (e.g., Hess Deep, Tyrrhenian Sea, Fig. 2 in Früh-Green et al., 2004) and are similar to our results.

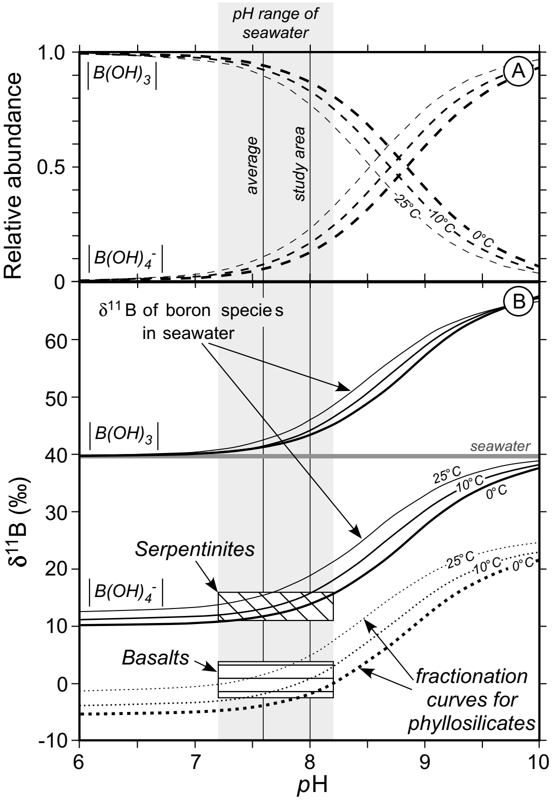

Fig. 9. Distribution of boric acid and borate in seawater (dashed curves in the part A of the diagram) and the theoretical relationship between the $\delta^{11}B$ values of boric acid and borate, and the seawater pH at $T = 0$, 10, and 25 °C (full curves in the part B of the diagram). Dotted lines represent the boron isotopic composition of serpentine in equilibrium with seawater. For comparison boxes of serpentinites (this study) and altered basalts (Smith et al., 1995) are also reported. See Appendix A for calculation details.

Because bulk rock O-isotope compositions reflect the relative proportions of minerals, their formation temperature, and the degree of isotopic exchange during alteration, it is likely that positive correlations between B content and O-isotope compositions (Bonatti et al., 1984) reflect a major control on B and ^{18}O enrichment by high modal contents of low-temperature phyllosilicates (e.g., palygorskite) that preferentially incorporate greater concentrations of B (Früh-Green et al., 2004). However, our results strongly suggest that serpentine can incorporate significant amounts of boron in its crystal structure at moderate temperatures as documented by other authors (Palmer, 1996; Savov et al., 2006).

5.2.2. B-uptake at transient pH and moderate temperature conditions

In high-temperature basaltic hydrothermal systems, fluid compositions are controlled by precipitation of anhydrite, Mg-OH silicates, and Mg-hydroxides that lead to a marked depletion in magnesium and SO_4 coupled with a decrease in pH (Seyfried and Bischoff, 1981; Wetzel and Schock, 2000; German and Von Damm, 2003). Models of fluid–rock interaction during low-temperature ridge flank hydrothermal alteration of the upper oceanic crust indicate that boron isotope composition of the fluids slightly increase by an average of 5.1‰ (from 39.5‰ to ~45‰), accompanied by a decrease in B concentration of ~7% (Smith et al., 1995). In ultramafic-hosted hydrothermal systems, after an initial decrease in pH during early, rock-dominated stages of alteration, progressive serpentinization at moderate temperatures results in an increase in pH and depletion in SiO_2, Mg, and Fe in the fluid (Seyfried and Dibble, 1980; Janecky and Seyfried, 1986; Wetzel and Schock, 2000). Depending on the solution pH, boron removal can be important at temperatures up to 200–300 °C (Seyfried et al., 1984); boron uptake in minerals is favored at alkaline conditions, inducing variable ^{11}B enrichment in the resulting fluid.

In Fig. 10, the $\delta^{11}B$ data field of the AM serpentinites is compared with calculated boron isotope compositions of serpentine in equilibrium with seawater at different temperatures and pH (see Appendix A for calculation details). During high-temperature peridotite–seawater interaction (200–300 °C), the pH of fluids initially decrease from seawater values (≈8) down to neutral–acidic values (pH 4–6; Janecky and Seyfried, 1986) and then, as serpentinization progresses, it increases reaching slightly alkaline values (alkaline by 0.5–2 units calculated at experimental temperature considering that at 200–300 °C the neutral pH 5.5 due to the lowering of K_w for water). At these conditions the boron species in the fluid are dominated by $B(OH)_3$ (70–100%) with minor amounts of $B(OH)_4^-$. Using isotopic fractionation factors extrapolated to temperatures of 150–250 °C (from data of Liu and Tossell, 2005), we calculated $\delta^{11}B$ of serpentine in equilibrium with seawater at different pH and T (Fig. 10).

As shown in Fig. 10, at pH between 4 and 8, the $\delta^{11}B$ range of AM serpentinites overlap the fractionation curves for serpentine at 150–250° and are consistent with temperature estimates of serpentinization using oxygen isotopes. The significant variation in $\delta^{11}B$ and the lack of correlation between $\delta^{11}B$ and $\delta^{18}O$ values can now be explained in terms of changes in pH. If we consider a fixed serpentinization temperature of 150 °C, then the entire range of $\delta^{11}B$ recorded in the AM serpentinites could be produced by a progressive pH change from 6 up to 8, which is consistent with experimental data by Janecky and Seyfried (1986). The positive correlation between $\delta^{11}B$ and B content (Fig. 5) agrees with the observation that the magnitude of B exchange during serpentinization is extremely sensitive to pH changes in solution (Seyfried and Dibble, 1980; Janecky and Seyfried, 1986).

A Rayleigh-type fractionation process can also be considered as a viable process of B isotope exchange during hydration, as proposed for alteration of oceanic basalts by Spivack and Edmond (1987). Such a process dictates that as an increment of seawater reacts with fresh mantle rocks, the B concentration of the water will decrease and its $\delta^{11}B$ will increase due to removal of boron from the dominant trigonal species in solution to the tetrahedral sites in serpentine minerals. If we hypothesize that increments of seawater progressively alter new fresh peridotite portions, and back-reaction with previously altered rocks does not occur, the net result will be the formation of sequential serpentinite domains characterized by progressively higher $\delta^{11}B$ values. Furthermore, the equation of Spivack and Edmond (1987) indicates that the lower the water/rock ratio, the higher is the $\delta^{11}B$ of the rock. However, this behavior is exactly the opposite of that observed in the AM serpentinites.

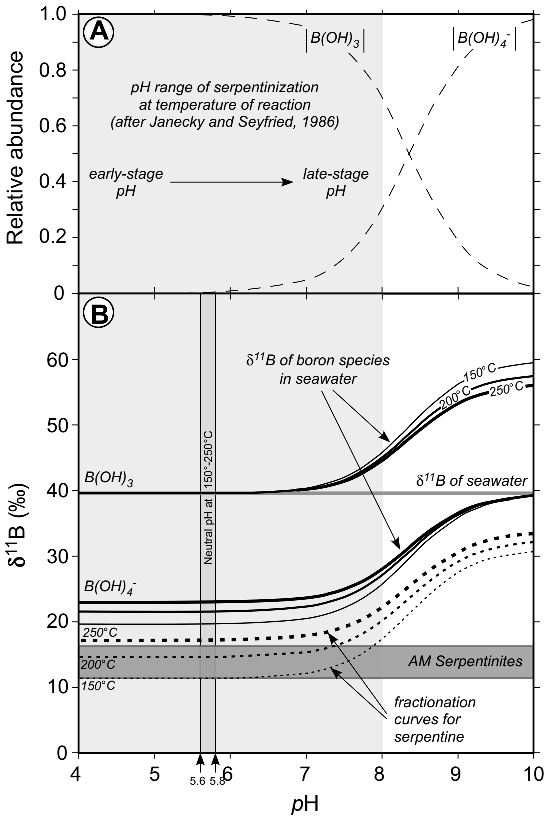

Fig. 10. Distribution of boric acid and borate in seawater (dashed curves in the part A of the diagram) and the theoretical relationship between the $\delta^{11}B$ values of boric acid and borate, and the seawater pH at $T = 150$, 200, and 250 °C (full curves in the part B of the diagram). Dotted lines represent the boron isotopic composition of serpentine in equilibrium with seawater. For comparison the serpentinite box is reported (from this study). See Appendix A for calculation details.

Two important points need to be considered to understand the B geochemistry of the AM serpentinites: (1) the high B content in the serpentinites indicates high water/rock ratios and a progressive B enrichment by removal of small amounts of B from multiple increments of seawater (in contrast, the total extraction of B from a single batch of seawater would give a serpentinite with $\delta^{11}B = 39.5‰$);

(2) the positive correlation observed between B content and δ^{11}B suggests that as water/rock ratios increase, the B content and δ^{11}B of the serpentinites become higher. In addition, all the AM serpentinites have consistently high to very high degrees of serpentinization and the observed variation of B content and δ^{11}B cannot simply be attributed to different modal amounts of serpentine minerals. The effect of transient pH conditions proposed above, coupled with variable water/rock ratios, could explain such behavior, in accordance with available experimental data (Seyfried and Dibble, 1980; Janecky and Seyfried, 1986).

Thus, we prefer a model where discrete portions of mantle rocks were sequentially hydrated by progressive seawater infiltration. The total B budget and the δ^{11}B of the circulating seawater were little modified and local isotopic equilibrium was attained, producing an overall constant offset between the δ^{11}B of serpentinites and seawater, with minor variations controlled by both water/rock ratios and transient pH conditions.

5.3. Fluid–rock ratios during serpentinization

The mineral assemblages and geochemical signatures of the AM serpentinites are the result of progressive serpentinization, predominantly under static conditions, during a long-lived history of seawater infiltration, alteration, and emplacement of the massif. Thus, the isotopic signatures of the rocks must be considered as an integrated signal of this history and will be influenced by reservoir type and sizes and degree of mass transfer during multiple or continuous phases of alteration.

In order to characterize the circulation processes, the amount of fluid that passed through the AM serpentinites has been estimated using the classic equations of Taylor (1974) modified by McCulloch et al. (1981). The effects of water–rock interaction on the combined isotopic systems of boron and strontium are shown in Fig. 11. According to the serpentinization history described above, the calculation was performed considering an “open system” in which multiple increments of seawater infiltrated the rock. Different combinations of pH for a temperature of 150 °C were used to show the variability in final δ^{11}B values that can be obtained. The shapes of the curves in Fig. 11 reflect the very low initial B content in harzburgites (here represented by the B content of depleted mantle) and show that the δ^{11}B signature of mantle rocks rapidly changes at relatively low water–rock ratios. For W/R ratios >0.1, the ^{87}Sr/^{86}Sr ratio becomes rapidly modified and combined boron–strontium isotope compositions coherent with serpentinites are reached at water/rock ratios of 100–800.

In a companion study of samples from the Lost City area collected in 2003 and 2005, Delacour et al. (2004) documents a range of Sr isotope compositions similar to our samples and shows that Nd isotope compositions are shifted to seawater-like values, with ε_{Nd} ranging from -4.7 to $+11.3$. Because Nd is essentially immobile, the Nd isotope composition of the oceanic crust remains unaffected except at very high W/R ratios (Michard et al., 1983; Michard and Albarede, 1986). Thus, the significant shift in B, Sr and Nd isotope compositions towards seawater values provide important constraints on the degree of seawater–rock interaction and time integrated water–rock (W/R) ra-

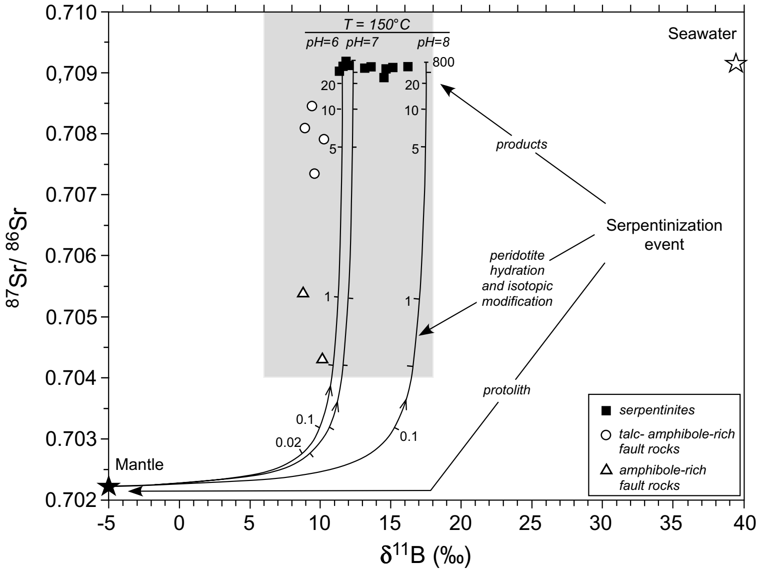

Fig. 11. ^{87}Sr/^{86}Sr versus δ^{11}B diagram for Atlantis Massif samples showing calculated water/rock interaction curves by using equations for open systems of McCulloch et al. (1981). The curves for seawater–peridotite interaction were calculated for $T = 150$ °C and three different pH values. Calculated curves (for any given pH) will shift to the right with increasing T. Calculation at higher temperatures (200–250 °C) fits with serpentinite samples having high δ^{11}B values. Parameters used in calculation are: (1) seawater, Sr = 8 ppm, ^{87}Sr/^{86}Sr = 0.70917, B = 4.5 ppm, δ^{11}B = 39.5‰; (2) harzburgites, Sr = 6 ppm, ^{87}Sr/^{86}Sr = 0.7022, B = 0.06 ppm, δ^{11}B = −5‰ (data from Spivack and Edmond, 1987; Chaussidon and Jambon, 1994; Salters and Stracke, 2004; Workman and Hart, 2005). Small numbers near the curves indicate the calculated W/R ratios.

tios (Hart et al., 1974; McCulloch et al., 1980; McCulloch et al., 1981; Kawahata and Scott, 1990; Gillis et al., 2005).

It is also important to note that the samples collected by dredging or submersibles for our studies represent the "outer skin" of this system and, thus, the end-product of long-lived tectonic and hydrothermal activity during formation and emplacement of the massif as a OCC. Therefore, the chemical signatures (used to infer T, fluxes, mass transfer, etc.) may not be fully representative of the present-day conditions (especially T) in the basement peridotites that directly feed the Lost City system. If one considers lithospheric cooling as the system ages, it is not surprising that the hydrogen isotope temperatures calculated from H_2–CH_4 in the vent fluids are slightly lower than those recorded in the serpentinites we sampled.

5.4. Silica metasomatism and boron loss

Field, petrographic and geochemical studies clearly indicate that the talc–amphibole-rich assemblage along the detachment fault zone formed by replacement of variably serpentinized peridotites (Boschi et al., 2006a; Karson et al., 2006). The precursory serpentinites are commonly preserved as centimeter-sized lenses wrapped by a talc schist foliation (Fig. 2) and contain local relics of primary peridotite minerals. Talc formation can be attributed to the simple reaction: Serpentine + 2 SiO_2 = Talc + H_2O, which is generally considered a prograde reaction taking place in the presence of SiO_2-rich fluids at temperatures of about 300–350 °C (at low-pressure, Evans and Trommsdorff, 1970; Bach et al., 2004; Manning, 2004). Although Si can be produced by serpentinization of pyroxene if the rate of pyroxene alteration is greater than that of olivine (Allen and Seyfried, 2003), Boschi et al. (2006a) argue, on the basis of petrographic and bulk rock geochemical data, that the Si-rich fluids leading to talc schist formation were evolved fluids derived from interaction of seawater with gabbroic rocks. The $^{87}Sr/^{86}Sr$ ratios of the talc-rich rocks are intermediate between the serpentinite and gabbro compositions, which provide further evidence that the Si-rich, high-T, low-pH fluids necessary to drive the serpentinite into the talc stability field were generated by interaction of seawater with mafic rocks (Bach et al., 2004).

Although the talc-rich rocks show similar $\delta^{18}O$ values to the serpentinites (Fig. 6), fractionation factors for talc–water and serpentine–water are different (Wenner and Taylor, 1973; Savin and Lee, 1988; Zheng, 1993; Saccocia et al., 2001). Thus, calculated temperatures of mineral–fluid equilibrium will differ: the talc-rich fault rocks yield equilibrium temperatures of 270–350 °C (assuming seawater with $\delta^{18}O$ of 0‰), which are higher than the integrated temperatures discussed above for progressive serpentinization (150–250 °C). Similarly, temperature calculations for the talc-rich rocks, using a fluid with a modified $\delta^{18}O$ value of 1–2‰ (consistent with the average black smoker vent fluid compositions; Shanks, 2001), enhance the differences and yield higher temperatures (330–450 °C) for talc metasomatism. The differences in temperature estimates may reflect the fact that Si-metasomatism was a single alteration event with little mineralogical or chemical change after formation of the talc–amphibole mineral assemblages.

Dehydration of serpentinite to talc-rich assemblages also has important implications on fluid circulation and element mobility along the detachment fault zone, in that approximately half of the structurally bound water in the system is remobilized (Boschi et al., 2006a; Fig. 3). In turn, the release of water-rich fluids during talc formation after serpentine seems to have strongly affected the behavior of B isotopes and B concentrations in the detachment system. The effects of B extraction during dehydration of serpentinite to talc-rich rocks can be evaluated by classic modeling of the two end-member equilibrium processes: (1) batch volatilization and (2) Rayleigh volatilization (Fig. 12).

The volatilization curves shown in Fig. 12 were calculated for $T = 300$ °C for initial serpentinite $\delta^{11}B$ values of 16.2‰ (sample 3639-1254C) and 13.2 ‰ (sample 3645-1159C), considering tetrahedrally coordinated B in serpentine and talc and the possibilities of tetrahedral and trigonal B speciation in the fluid. The metasomatic talc- amphibole-rich rims (samples 3639-1254R and 3645-1159R) have been plotted using the measured $\delta^{11}B$ and the calculated mole fraction of B that remains in the rock ($F = B_{rim}/B_{core}$). The F values of two additional talc-rich metasomatic rocks (3642-1309 and D4-4) were calculated by using the average B content of serpentinites and then plotted in Fig. 12.

The entire sample set plot in the upper part of the diagram showing relatively small isotopic fractionations with respect to the original serpentinite values and suggest a dominantly tetrahedral speciation of B into the fluid. Dehydration of serpentinite to talc-rich assemblages removes much of the B, leaving less than 50% of the original B budget in the metasomatic rocks. The talc-rich rim of sample 3639-1254 plots close to the calculated Rayleigh volatilization curve for its serpentinite core, while the talc-rich rim of sample 3645-1159 shows an intermediate position between

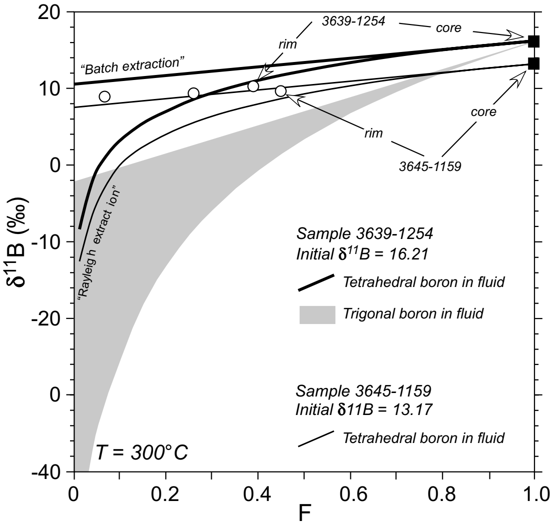

Fig. 12. Calculated curves for batch and Rayleigh fractionation at 300 °C for boron extraction during talc metasomatism of serpentinite. Open circles are talc-rich fault rocks; error bars for $\delta^{11}B$ inside symbol. See text for detailed discussion.

the Rayleigh and Batch curves calculated for its serpentinite core. Such behavior is commonly observed in natural processes (Baumgartner and Valley, 2001) and indicates an intermittent role of both open and closed system conditions. As clearly shown by the gray shaded area in Fig. 12, boron extraction by trigonal species in the fluids would produce large isotope fractionations that are not compatible with our data. In summary, dehydration of serpentinites driven by talc metasomatism produces alkaline fluids, stabilizing aqueous $B(OH)_4^-$ that in turn limit the extent of B isotope fractionation between the protolith, the fluid, and the metasomatic assemblage.

Integration of B with Sr isotope data can help in deciphering the complex interaction between external fluids (partially equilibrated with gabbroic rocks) and internal fluids (dehydration of serpentinite) along the detachment. Water/rock ratio estimates by Sr isotope data were made (open system conditions; McCulloch et al., 1981) considering a fluid with 10 ppm of Sr and $^{87}Sr/^{86}Sr$ of 0.705, reacting with the serpentinites ($Sr = 2–4$ ppm; $^{87}Sr/^{86}Sr = 0.70917$). The Sr isotope composition of talc-rich rocks is reached for water/rock values in the range 0.2–0.7 indicating that fluid flow, although tectonically focused into the DSZ, did not involve significantly large fluxes of water as is inferred for serpentinization of the AM peridotites. In Fig. 13, the infiltration of low $^{87}Sr/^{86}Sr$, Si-rich fluids, and the loss/isotope fractionation of B are combined to model the complex interaction between fluids and serpentinites during talc metasomatism. Sr isotope data indicate that the equilibration of infiltrating fluids with the amphibole-rich fault rocks produce a realistic input fluid for talc formation. The interaction of this modified fluid with serpentinites is qualitatively illustrated by the curves in Fig. 13 that have been obtained joining the calculated $^{87}Sr/^{86}Sr$ (at different water/rock ratios) and $\delta^{11}B$ (for rocks progressively depleted in B; Fig. 12) of the metasomatic rocks. It is important to note that the theoretical path from serpentinites to talc-rich rocks in $^{87}Sr/^{86}Sr–\delta^{11}B$ space could be modeled in a number of combinations because the temporal correlation between the two processes cannot be constrained.

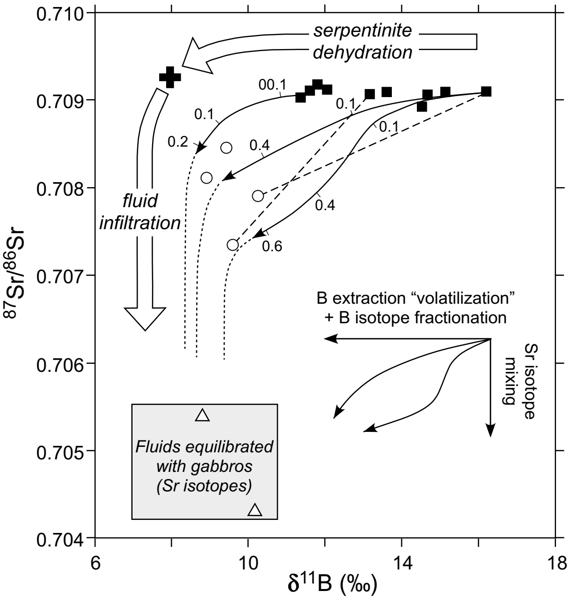

Fig. 13. Diagram showing the combined effect of serpentinite dehydration (B extraction and fractionation) and infiltration of a Si-rich fluid (Sr isotope mixing) in equilibrium with gabbros ($Sr = 10$ ppm, $^{87}Sr/^{86}Sr = 0.705$); see text for detailed discussion. Small numbers near the curves indicate the calculated W/R ratios.

5.5. Implications for behavior of boron during subduction of serpentinites

Relative to MORB and OIB, volcanic arc rocks display high-boron concentrations, generally heavier isotopic compositions and typical front- to back-arc boron and $\delta^{11}B$ trends ($+8‰ > \delta^{11}B > -8‰$; see Morris et al., 1990; Ryan and Langmuir, 1993; Ishikawa and Tera, 1999; Rosner et al., 2003, and references therein), which indicate transport of B from subducted sediments and hydrothermally altered oceanic crust into the mantle wedge (Palmer, 1991; Ishikawa and Nakamura, 1994; Morris and Ryan, 2003). It is widely accepted that B behaves incompatibly during subduction and is strongly partitioned into the fluid phase during dewatering of sediments and dehydration of altered basaltic crust (Morris and Ryan, 2003). However, the B isotope data from Mariana serpentinite seamounts (Benton et al., 2001) indicate that the two-component mixing model of Ishikawa and Tera (1999) does not explain the complete range of $\delta^{11}B$ values observed from forearc fluids to inner arc magmas (from +13‰ to −8‰). Instead, some degree of B isotope fractionation and/or additional components (B from subducted serpentinites) is required and the trend probably reflects a continuous input of B from a slab that is evolving isotopically.

There is a strong interest in modeling boron elemental and isotopic mass balance in subduction zones, and several authors suggest that only 20–30% of the input to the trench inventory of boron can be accounted for by the magmatic outputs of volcanic arcs (Morris and Ryan, 2003), while fluid released in the forearc–trench area can account for another 10–50% of the input budget (You et al., 1995; Savov et al., 2005a). Thus, at least 30% of the B subducted in sediments and altered oceanic crust is not accounted for by known arc and trench outputs. Moreover, the study of metasedimentary rocks (Bebout et al., 1999) indicates that most of the boron in subducted sediments is rapidly removed before the system reaches the appropriate depths under arc volcanic fronts. Such behavior raises questions about the ultimate reservoir controlling the enrichment of B in arc magmas.

Although it has been suggested that release of H_2O during serpentinite dehydration may govern certain physical processes in subduction zones, a number of recent studies emphasize the unique geochemical imprint that fluids released during serpentinite dehydration may impart on subduction zone magmas (Fryer, 1992; Scambelluri et al., 2004; Tenthorey and Hermann, 2004). In particular, two distinct types of serpentinites have the potential to affect the B across-arc budget: those belonging to the subducted oceanic lithosphere, and those produced in the mantle wedges. The former represent the result of oceanic lithosphere hydration, occurring at ridge-transform intersections (like the AM serpentinites), along nonvolcanic slow- and ultra slow-spreading ridges (Seyler et al., 2003; Cannat et al., 2006), and/or at the bend of subducting plates (Ranero et al., 2003; Ranero and Sallarès, 2004). On the other hand, several authors (Benton et al., 2001; Hattori and Guillot, 2003; Savov et al., 2005a; Savov et al., 2007) propose that water, and mobile elements like B, released during the early stages of subduction by sediments (forearc region), migrate upward and hydrate the mantle wedge to form a serpentinite layer along and just above the subducting slabs, which can be dragged downward by mantle flow. Such processes involving a hydrated mantle wedge are believed to be responsible for the formation of the serpentinite mud volcanoes occurring in the forearc region of the Mariana subduction zone (Benton et al., 2001; Savov et al., 2007). Regardless of the serpentinite type involved in subduction, serpentine minerals are relatively stable up to 500–700 °C at 2.5–4.5 GPa (Ulmer and Trommsdorff, 1995), and serpentinites can release water and boron to the mantle wedge in the root zone of the arc magmatic systems (e.g., Tonarini et al., 2007). Addition of this third component to the classic two-component model (Palmer, 1991; Ishikawa and Nakamura, 1994) provides a better explanation of the B isotopic data in subduction settings.

As discussed previously, the Atlantis Massif represents a good example where early stages of peridotite hydration (serpentinization) are locally followed by serpentinite dehydration (producing talc-rich rocks) driven by fluid infiltration and shearing along a detachment fault. The coupled effect of infiltration of Si-rich fluids with dehydration of serpentine minerals during formation of talc-rich rocks induces a marked B depletion but little B isotopic fractionation. In the Atlantis Massif, the occurrence of Si-rich fluids was controlled by the local geological setting and could be considered a minor feature with respect to the large volume of seawater involved in serpentinization. However, in subduction zones, Si-rich fluids released by metasediments (Manning, 2004) must be considered a primary factor controlling element removal from the slab and making them available for mantle metasomatism. Evidence for Si-metasomatism of ultramafic rocks is reported by King et al. (2003) from a tectonic mélange of the Franciscan complex, California. These authors describe replacement of serpentinites by talc and amphibole assemblages that occurred at estimated temperature of 450–500 °C. Interaction at $T > \sim 300$°C between Si-rich fluids and serpentinites in both the subducting slab and the hydrated mantle wedge could produce talc metasomatism and a significant release of B-rich fluids with high δ^{11}B value. This reaction could play a role in the range 300–500 °C after the first main extraction of B from sediments and before the high-T extraction of B from serpentinites (below the arc) controlled by the total dehydration of serpentine. Our data indicates that the formation of talc effectively removes B, producing a fluid enriched in ^{11}B and leaving a metasomatic rock depleted in B and with a lighter B isotopic composition. The B isotope composition of the resulting fluids calculated for initial δ^{11}B in serpentinites of 8–16‰ (data from this study and Spivack and Edmond, 1987) and temperatures of 300–500 °C varies in the range ~20–30‰ and ~12–20‰, respectively, in the case that boron in the fluid is trigonally or tetrahedrally coordinated (calculated by both Rayleigh and batch volatilization methods). Such heavy compositions when mixed with the lighter fluids coming from subducted metasediments (already fractionated in the forearc region) can also explain observed variations in arc to backarc magmatic rocks.

Serpentinites are relatively common at slow- and ultra-slow-spreading ridge environments, whereas they are rare in the Pacific and their role in present day subduction processes is limited. However, serpentinization in off-axis environments, in the mantle wedge and as plates bend at trenches has been discussed by several authors (e.g., Hattori and Guillot, 2003; Ranero et al., 2003; Ranero and Sallarès, 2004); thus, the role of serpentinites in present-day subduction zone systems must be considered relevant. In addition, oceanic serpentinites involved in subduction zones are common in past collisional settings (such as the Alpine and Himalayan system) and their contribution to the geochemical signature of the related magmatism cannot be ignored.

6. CONCLUSIONS

The 1.5 Ma old Atlantis Massif is one of the best-documented OCCs along the Mid-Atlantic Ridge and hosts the off-axis, low-temperature Lost City Hydrothermal Field. Extensive field sampling of this system provided the opportunity to study the evolution of an ultramafic-hosted hydrothermal system under conditions ranging from near-axis to off-axis. Boron concentrations and isotopic compositions, coupled with Sr isotopes, bulk rock geochemistry, and petrography provide new insights into the physical and chemical conditions attained by hydrothermal fluids during serpentinization and metasomatism. From our studies, we draw the following conclusions:

(1) Formation of the relatively young AM serpentinites occurred at integrated temperatures of 150–250 °C under high water/rock ratios and led to a marked enrichment in B from seawater. Calculations based on Sr isotope ratios yield water/rock ratios of ~100–800. Changes in pH produced a variable δ^{11}B signature, with increasing pH resulting in higher B contents and progressively higher δ^{11}B values.

(2) The AM serpentinites show no significant elemental or B, O, and Sr isotope signatures of seafloor weathering or carbonate precipitation, and we conclude that low-temperature alteration and carbonate uptake are insignificant for the Sr, B, and O geochemistry of the Atlantis Massif serpentinites.

(3) Strontium isotope compositions of the talc-rich fault rocks indicate that talc metasomatism along the detachment fault occurred at low water/rock ratios (0.2–0.7) and reflect interaction with Si-rich, evolved fluids with a mafic component derived from interaction with gabbro lenses within a peridotite-dominated ridge segment.

(4) Talc metasomatism is coupled to dehydration of serpentinites and is marked by B depletion and isotopic fractionation. The extent of isotopic fractionation between serpentine- and talc-rich rocks indicate that B was removed as $B(OH)_4^-$ under alkaline conditions.

(5) Our study highlights the complex links between tectonic processes and hydrothermal activity recorded in the basement of the AM prior to and during the development of the LCHF. Boron and strontium isotope signatures together with calculated water/rock ratios of the serpentinites and talc-rich fault rocks suggest that hydrothermal circulation in the Atlantis Massif strongly varied in response to evolving tectonic conditions. Pervasive serpentinization reflects long-lived seawater infiltration along widespread microfracture networks that developed during progressive uplift, exhumation, and hydrothermal activity facilitated by normal and low-angle faulting and volume expansion associated with serpentinization. In contrast, talc metasomatism reflects limited amounts of hydrothermal fluids channeled within the detachment fault. Interaction of seawater with gabbroic lenses and dehydration of the serpentinite resulted in distinct isotopic and chemical signatures in the talc-rich rocks and extraction of B from the serpentinites.

(6) The observed B isotope fractionation during talc metasomatism of serpentinites has implications for understanding the behavior of boron in subduction zones and the observed across-arc boron isotopic signature of magmas. Our study suggests that B removal and isotopic fractionation accompanying talc formation in subducted serpentinite slabs or hydrated mantle wedges may play an important role in the mobilization of B-rich fluids with high $\delta^{11}B$ values at temperatures of 300–500 °C.

We anticipate that future studies and the comparison of data from active and fossil systems will provide a more comprehensive picture of the variations and controls on the physical–chemical conditions of fluid–rock interaction during the progressive evolution of long-lived ultramafic-hosted hydrothermal systems.

ACKNOWLEDGMENTS

We thank the ship crews and scientific parties involved in the investigations to the Atlantis Massif in 2000 and 2003 (cruises AT3-60 and AT7-34) for their support and input to this project. We also acknowledge Sonia Tonarini for helpful discussions and important suggestions. We thank NOAA Ocean Exploration Program (Lost City 2005) and Bob Ballard for providing additional samples and images of key outcrops. This manuscript benefited greatly from anonymous reviews of an earlier version and by thorough, constructive comments from I. Savov, W.P. Leeman and an anonymous reviewer of the revised version. We also thank associate editor J. Alt for thoughtful comments and help with improvements. This work was supported by ETH Grant 0-20890-01 and Swiss SNF Grants 2100-068055 and 200020-107620 to G.L. Früh-Green and NSF Grant OCE0137206 to D.S. Kelley. A. Dini spent a month at ETH Zurich, Department of Earth Sciences, for discussion and analytical work, supported by the CNR—“Short-Term Mobility” program (May 2005).

APPENDIX A. BORON SPECIATION, ISOTOPE FRACTIONATION FACTORS, AND CALCULATION OF PH–Δ^{11}B–X DIAGRAMS

Boron has no natural redox chemistry. Fractionation between the two isotopes (^{10}B and ^{11}B) is almost entirely controlled by their relative partitioning between trigonal (BO_3, $B(OH)_3$) and tetrahedral (BO_4, $B(OH)_4^-$) species: ^{11}B with its lower vibrational energy is preferentially partitioned into the high ionic potential trigonal species, whereas the higher vibrational energy of ^{10}B favors uptake into the lower ionic potential tetrahedral species (Kakihana et al., 1977). Boron isotope fractionation is commonly expressed by the fractionation factor $\alpha_{III-IV} = (^{11}B/^{10}B)_{trigonal}/(^{11}B/^{10}B)_{tetrahedral}$. The variation of α_{III-IV} is inversely dependent on temperature, roughly ranging from ≈ 1.004 at high-temperatures up to ≈ 1.030 at low-temperatures. This relationship results in the wide variation of boron isotope compositions observed in nature ($-40‰ < \delta^{11}B < +60‰$; where $\delta^{11}B = \{[(^{11}B/^{10}B)_{sample}/(^{11}B/^{10}B)_{std\ SRM\ 951}] - 1\} \times 10^3$).

Boron isotope fractionation factors for most phases have not been determined experimentally, and theoretical semi-empirical values calculated by Kakihana et al. (1977) are widely used in the literature (Palmer and Swihart, 1996 and references therein). However, many studies on natural rocks and fluids have shown systematic downward offsets of $\delta^{11}B$ values from this theoretical curve (e.g., Spivack and Edmond, 1987). Recent determinations of fractionation factors by ab-initio calculation (Oi, 2000; Liu and Tossell, 2005; Zeebe, 2005), while confirming the coordination effect and the great variation with temperature, provide larger fractionation factors that provide a better fit with natural occurrences. The calculated α values vary depending on spectroscopic data, the calculation method, and on the structural arrangement of the next nearest neighbor atoms (influencing the B–O bonding/frequency). Liu and Tossell (2005) found that the four-coordinated BO_4 bonding (or vibration) in silicate minerals is substantially different from that in $B(OH)_4^-$ in a fluid. Thus, fractionation data for $B(OH)_4^-$ cannot be applied to BO_4 tetrahedral groups in minerals and boron isotopic fractionation occurs during both trigonal–tetrahedral and tetrahedral$_{fluid}$–tetrahedral$_{mineral}$ exchange. This behavior has recently been confirmed by boron isotope partitioning experiments between mica and fluids carried out by Wunder et al. (2005). Our interpretation of boron isotope data of AM serpentinites is based on the paper of Liu and Tossell (2005) because it provides a coherent calculated fractionation factor dataset for boron species in seawater and between fluids and minerals. Clearly, however, a definitive experimental determination of fractionation factors is needed.

Dissolved boron in seawater is dominated by mononuclear species $B(OH)_3$ (boric acid; trigonally coordinated) and $B(OH)_4^-$ (borate; tetrahedrally coordinated), and due to the relatively low seawater B concentration (about 0.416 mmol/kg^{-1} or 4.5 ppm), polynuclear species are absent (Byrne and Kester, 1974). This is true also at hydrothermal conditions because the proportion of polynuclear species becomes increasingly low at higher temperatures (Mesmer et al., 1972). Distribution of $B(OH)_3$ and $B(OH)_4{}^-$ in seawater and hydrothermal solutions has been calculated as a function of pH and T using available values of the apparent dissociation constant of boric acid (K^*_B) and the Eq. (1):

$$\log\left(\frac{B(OH)_4^-}{B(OH)_3}\right) = \mathrm{pH} - \mathrm{p}K^*_B \tag{1}$$

where $\mathrm{p}K^*_B = -\log(K^*_B)$.

The $\mathrm{p}K^*_B$ is significantly affected by both temperature and ionic strength/salinity of the solution (Hershey et al., 1986; Mesmer et al., 1988; Wofford et al., 1998) and is also strictly correlated with the self-ionization of water (quantified by $\mathrm{p}K_W$, whose half value is the pH of water or "neutral" pH; Mesmer et al., 1988; Yagasaki et al., 2005). Both $\mathrm{p}K_W$ and $\mathrm{p}K^*_B$ exhibit nonmonotonic temperature dependance, that is, they first decrease between 0 and 100–250 °C (respectively, from 14.2 to 11.2 and from 9.5 to 8.9 at low-pressure) and then increase as temperature approaches the supercritical region (e.g., up to $\mathrm{p}K_W \approx 14$ and $\mathrm{p}K^*_B \approx 11$ at 400 °C and 33 MPa). A moderate increase in solution salinity (and ionic strength) decreases the dissociation constant of boric acid such that the $\mathrm{p}K^*_B$ value of seawater at $T = 0$ °C is 8.85 (Dickson, 1990).

Speciation of dissolved boron in seawater at temperature of 0, 10, and 25 °C (Fig. 9) was calculated over the whole pH range using Eq. (1) and $\mathrm{p}K^*_B$ values of 8.85, 8.71, and 8.53, respectively, provided by Dickson (1990). At higher temperatures, as those inferred for serpentinization (150–250 °C), experimental $\mathrm{p}K^*_B$ values of seawater are not available but they should not differ significantly from the value of $\mathrm{p}K^*_B$ of seawater at 45 °C (8.30; Dickson, 1990) because, by similarity with $\mathrm{p}K^*_B$ of pure water, the major decrease occurs in the 0–50 °C range and then the $\mathrm{p}K^*_B$ values reach a large minimum up to 200 °C (Mesmer et al., 1988). On the other hand, it is well known that over 150 °C seawater undergoes strong modification due to the combined effect of precipitation of Mg and Ca sulfates/hydroxy-sulfates and Na removal by interaction with the oceanic crust (German and Von Damm, 2003). In this case the salinity of seawater is strongly reduced and the resulting Cl-rich hydrothermal fluid should have a $\mathrm{p}K^*_B$ value between those of seawater and pure water (between 8.3 and 9.0–9.3; Mesmer et al., 1988). The $\mathrm{p}K^*_B$ increase shifts to the left the speciation and $\delta^{11}B$ curves in Fig. 9 by about one pH unit as a maximum, but does not affect the general significance of the diagram. Furthermore, several geochemical and isotopic considerations suggest that the ingress of seawater during serpentinization was rapid with negligible interaction with the oceanic crust, potentially leaving its overall chemical composition undisturbed.

After calculating the speciation curves shown in Figs. 9 and 10, the boron isotope composition of $B(OH)_3$ and $B(OH)_4^-$ species in seawater and four-coordinated BO_4 in serpentine structure were calculated using isotope equilibrium constants extrapolated by fitting data provided by Liu and Tossell (2005). Three equations have been obtained:

$$1000 * \mathrm{Ln}\alpha_{\mathrm{IIIsw-IVsw}} = 7.2087 * (1000/K) + 2.3467 \tag{2}$$

$R^2 = 0.9839$ for fractionation between $B(OH)_3$ and $B(OH)_4{}^-$ in seawater,

$$1000 * \mathrm{Ln}\alpha_{\mathrm{IIIsw-IVmin}} = 13.43 * (1000/K) + 4.7093 \tag{3}$$

$R^2 = 0.9988$ for fractionation between $B(OH)_3$ in seawater and $(BO)_4$ in a phyllosilicate

$$1000 * \mathrm{Ln}\alpha_{\mathrm{IVsw-IVmin}} = 5.0225 * (1000/K) + 3.1553 \tag{4}$$

$R^2 = 0.9995$ for fractionation between $B(OH)_4{}^-$ in seawater and $(BO)_4$ in a phyllosilicate.

In the case of Eq. (2) the fitted dataset is represented by four values of isotope equilibrium constants at 0, 25, 40, and 60 °C, while the last two equations are calculated each on the basis of three points at 25, 60, and 300 °C. The most relevant uncertainty is due to the extrapolation of Eq. (2) at the relatively high-temperature inferred for serpentinization (150–250 °C) and Si-metasomatism (350 °C). Moreover, isotopic fractionation factors between boron species in seawater and phyllosilicate were calculated by Liu and Tossell (2005) for a mica-like structure fragment, and their applicability to serpentine minerals still await confirmation. However, their data represent the most unique, consistent boron isotope fractionation set available for both aqueous–aqueous and aqueous–mineral boron species and, in our opinion, represent a better choice with respect to the use of fractionation factors from Kakihana et al. (1977).

The boron isotope compositions of $B(OH)_3$ and $B(OH)_4{}^-$ species in seawater at different pH and T were calculated by using the following equations (see Pagani et al., 2005 for a detailed discussion):

$$R_{B(OH)_4^-} = R_{SW}\left(\frac{1 + \alpha_{\mathrm{IV-III}}10^{\mathrm{p}K^*_B - \mathrm{pH}}}{1 + 10^{\mathrm{p}K^*_B - \mathrm{pH}}}\right) \tag{5}$$

$$R_{B(OH)_3} = \frac{R_{B(OH)_4^-}}{\alpha_{\mathrm{IV-III}}} \tag{6}$$

where R_{SW} is the $^{11}B/^{10}B$ ratio of seawater (4.2034; $\delta^{11}B = 39.5‰$) and $\alpha_{\mathrm{IV-III}} = 1/\alpha_{\mathrm{III-IV}}$ the fractionation factor at the temperature of interest. $^{11}B/^{10}B$ ratios were converted to $\delta^{11}B$ notation for plotting in Figs. 9 and 10. Finally, the $\delta^{11}B$ values of serpentine in equilibrium with both $B(OH)_3$ and $B(OH)_4{}^-$ species in seawater were calculated:

$$\delta^{11}B_{\mathrm{serp}(1)} = \left\{\frac{(1000 + \delta^{11}B_{B(OH)_3})}{\alpha_{\mathrm{III_{sw}-IV_{serp}}}}\right\} - 1000 \tag{7}$$

$$\delta^{11}B_{\mathrm{serp}(2)} = \left\{\frac{(1000 + \delta^{11}B_{B(OH)_4^-})}{\alpha_{\mathrm{IV_{sw}-IV_{serp}}}}\right\} - 1000 \tag{8}$$

At low-temperature the two calculations give the same result, but for increasing temperature, the two estimates diverge up to a maximum of 2‰ around 300 °C. This is probably due to the poor fitting of Eq. (2) and the lack of data at high-T for fractionation factors between $B(OH)_3$ and $B(OH)_4{}^-$ in seawater (Liu and Tossell, 2005). Each boron isotope composition curve for serpentine in Fig. 10 (at $T = 150$, 200, and 250 °C) represents the average of the two estimates.

REFERENCES

Allen D. E. and Seyfried W. E. (2003) Compositional controls on vent fluids from ultramafic-hosted hydrothermal systems at mid-ocean ridges: an experimental study at 400 °C, 500 bars. *Geochim. Cosmochim. Acta* **67**(8), 1531–1542.

Allen D. E. and Seyfried W. E. (2004) Serpentinization and heat generation: constraints from Lost City and Rainbow hydrothermal systems. *Geochim. Cosmochim. Acta* **68**, 1347–1354.

Alt J. C. and Shanks W. C. (2003) Serpentinization of abyssal peridotites from the MARK area, Mid-Atlantic Ridge: sulfur geochemistry and reaction modelling. *Geochim. Cosmochim. Acta* **67**, 641–653.

Alt J. C. and Shanks W. C. (2006) Stable isotope compositions of serpentinite seamounts in the Mariana forearc: serpentinization processes, fluid sources and sulfur metasomatism. *Earth Planet. Sci. Lett.* **242**, 272–285.

Bach W., Garrido C. J., Paulick H., Harvey J. and Rosner M. (2004) Seawater–peridotite interactions: first insights from ODP Leg 209, Mar 15°N. *Geochem. Geophys. Geosys.* **5**(9). doi:10.1029/2004GC000744.

Baumgartner L. P. and Valley J. W. (2001) Stable isotope transport and contact metamorphic fluid flow. In *Stable Isotope Geochemistry* (eds. J. W. Valley and D. R. Cole). *Rev. Min. Geochem.* **43**, pp. 415–467.

Bebout G., Ryan J. G., Leeman W. P. and Bebout A. (1999) Fractionation of trace elements by subduction-zone metamorphism—effect of convergent-margin thermal evolution. *Earth Planet. Sci. Lett.* **171**, 63–81.

Benton L. D., Ryan J. G. and Tera F. (2001) Boron isotope systematics of slab fluids as inferred from a serpentinite seamount, Mariana forearc. *Earth Planet. Sci. Lett.* **187**, 273–282.

Blackman D. K., Cann J. R., Janssen B. and Smith D. K. (1998) Origin of extensional core complexes: evidences from the Mid-Atlantic Ridge at Atlantis fracture zone. *J. Geophys. Res.* **103**, 21315–21333.

Blackman D. K., Karson J. A., Kelley D. S., Cann J. R., Früh-Green G. L., Gee J. S., Hurst S. D., John B. E., Morgan J., Nooner S. L., Ross D. K., Schroeder T. J. and Williams E. A. (2002) Geology of the Atlantis Massif (Mid-Atlantic Ridge, 30°N): implications for the evolution of an ultramafic oceanic core complex. *Mar. Geophys. Res.* **23**, 443–469.

Blackman D. K., Ildefonse B., John B. E., Ohara Y., Miller D. J., MacLeod C. J., and the Expedition 304/305 Scientists (2006) *Proceedings Integrated Ocean Drilling Program*, 304/305. College Station TX (Integrated Ocean Drilling Program Management International, Inc.), doi:10.2204/iodp.proc.304305.2006.

Blusztajn J. and Hart S. R. (1996) Sr and O isotopic ratios of aragonite veins from site 895. In *Proceedings of ODP, Sci. Results* (C. Mével, K.M. Gillis, J.F. Allan and P.S. Meyer). Ocean Drilling Program, College Station, TX, **147**, pp. 311–313.

Bonatti E., Lawrence J. R. and Morandi N. (1984) Serpentinization of ocean-floor peridotites: temperature dependence on mineralogy and boron content. *Earth Planet. Sci. Lett.* **70**, 88–94.

Bonatti E., Lawrence J. R., Hamlyn P. R. and Breger D. (1980) Aragonite from deep sea ultramafic rocks. *Geochim. Cosmochim. Acta* **44**, 1207–1214.

Bonatti E., Simmons E. C., Breger D., Hamlyn P. R. and Lawrence J. R. (1983) Ultramafic rock/seawater interaction in the ocean crust: Mg-silicate (sepiolite) deposition from the Indian Ocean floor. *Earth Planet. Sci. Lett.* **62**, 229–238.

Boschi C., Früh-Green G. L., Karson J. A., Kelley D. S. and Delacour A. (2006a) Mass transfer and fluid flow during detachment faulting and development of an oceanic core complex, Atlantis Massif (MAR 30°N). *Geochem. Geophys. Geosys.* **7**, Q01004. doi:10.1029/2005GC001074.

Boschi C., Früh-Green G. L. and Escartín J. (2006b) Occurrence and significance of serpentinite-hosted, talc-rich fault rocks in modern oceanic settings and ophiolite complexes. *Ofioliti* **31**(2), 129–140.

Brazelton W. J., Schrenk M. O., Kelley D. S. and Baross J. A. (2006) Methane- and sulfur-metabolizing microbial communities dominate the Lost City Hydrothermal Field Ecosystem. *Appl. Environ. Microbiol.* **72**, 6257–6270.

Byrne, Jr., R. H. and Kester D. R. (1974) Inorganic speciation of boron in seawater. *J. Mar. Res.* **32**, 119–127.

Campbell A. C., Palmer M. R., Klinkhammer G. P., Bowers T. S., Edmond J. M., Lawrence J. R., Casey J. F., Thompson G., Humphris S., Rona P. and Karson J. A. (1988) Chemistry of hot springs on the Mid-Atlantic Ridge. *Nature* **335**, 514–519.

Cann J. R., Blackman D. K., Smith D. K., McAllister E., Janssen B., Mello S., Avgerinos E., Pascoe A. R. and Escartín J. (1997) Corrugated slip surfaces formed at ridge–transform intersections on the Mid-Atlantic Ridge. *Nature* **385**, 329–332.

Cannat M. (1993) Emplacement of mantle rocks in the seafloor at mid-ocean ridges. *J. Geophys. Res.* **98**, 4163–4172.

Cannat M., Sauter D., Mendel V., Ruellan E., Okino K., Escartin J., Combier V. and Baala M. (2006) Modes of seafloor generation at a melt-poor ultraslow-spreading ridge. *Geology* **34**, 605–608.

Catanzaro E. J., Champion C. E., Garner E. L., Marinenko G., Sappenfield K. M. and Shields W. R. (1970) Boric acid; isotopic and assay standard reference materials. *National Bur. Standards (US) Spec. Publ.* **260-17**, 70.

Chaussidon M. and Jambon A. (1994) Boron content and isotopic composition of oceanic basalts: geochemical and cosmochemical implications. *Earth Planet. Sci. Lett.* **121**, 277–291.

Delacour A., Früh -Green G. L., Frank M., Bernasconi S.M., Boschi C. and Kelley D. S. (2004) Fluid–rock interaction in the basement of the Lost City Vent Field: insights from stable and radiogenic isotopes. *Eos Trans. AGU* **85**(47), Fall Meeting Suppl., #B13A-0198 (abstr.).

Delacour A., Früh-Green G. L., Bernasconi S. M., Schaeffer P., Frank M., Gutjahr M. and Kelley D. S. (2007) Influence of high fluid fluxes on sulfur and carbon speciation of serpentinites of the Atlantis Massif. *Geophysical Research Abstracts* **9**, 03097, EUG.

Dickson A. G. (1990) Thermodynamics of the dissociation of boric acid in synthetic seawater from 273.15 to 318.15 K. *Deep-Sea Res.* **37**, 755–766.

Edmond J. M., Measures C., McDuff R. E., Chan L. H., Collier R. and Grant B. (1979) Ridge crest hydrothermal activity and the balances of the major and minor elements in the ocean; the Galapagos data. *Earth Planet. Sci. Lett.* **46**(1), 1–18.

Evans B. W. and Trommsdorff V. (1970) Regional metamorphism of ultramafic rocks in the Central Alps; parageneses in the system CaO–MgO–SiO$_2$–H$_2$O. *Bull. Suisse Mineral. Petrog.* **50**(3), 481–492.

Fallick A. E., Macaulay C. I. and Haszeldine R. S. (1993) Implications of linearly correlated oxygen and hydrogen isotopic compositions for kaolinite and illite in the Magnus Sandstone. *Clays Clay Miner.* **41**, 184–190.

Fisher A. T. and Becker K. (2000) Reconciling heat flow and permeability data with a model of channelized flow in oceanic crust. *Nature* **403**, 71–74.

Forneris J. F. and Holloway J. R. (2003) Phase equilibria in subducting basaltic crust: implications for H$_2$O release from the slab. *Earth Planet. Sci. Lett.* **214**(1–2), 187–201.

Früh-Green G. L., Plas A. and Lécuyer C. (1996) Petrologic and stable isotope constraints on hydrothermal alteration and serpentinization of the EPR shallow mantle at Hess Deep (Site 895). *Proc. ODP Sci. Res.* **147**, 255–293.

Früh-Green G. L., Connolly J. A. D., Plas A., Kelley D. S. and Grobéty B. (2004) Serpentinization of oceanic peridotites: implications for geochemical cycles and biological activity. In *The Subseafloor Biosphere at Mid-ocean Ridges, Geophys. Monogr. Ser.* **144** (eds. W. S. D Wilcock et al.). AGU, Washington, DC, pp. 119–136.

Früh-Green G. L., Kelley D. S., Bernasconi S. M., Karson J. A., Ludwig K. A., Butterfield D. A., Boschi C. and Proskurowski G. (2003) 30,000 Years of hydrothermal activity at the Lost City Vent Field. *Science* **301**, 495–498.

Früh-Green G. L., Delacour A., Boschi C., Bernasconi S. M., Butterfield D.A., Kelley D. S. and Proskurowski G. (2007) Building Lost City: serpentinization, mass transfer and life in a peridotite-hosted hydrothermal system. *Geochim. Cosmochim. Acta* **71/15**(Suppl 1), A298.

Fryer P. (1992) A synthesis of Leg 125 drilling of serpentinite seamounts on the Mariana and Izu-Bonin forearcs. In *Proceedings of ODP, Sci. Results* (P. Fryer, J.A. Pearce, L.B. Stokking). Ocean Drilling Program, College Station, TX, **125**, pp. 593–614.

Fryer P., Gharib J., Ross K., Savov I. P. and Mottl M. J. (2006) Variability in serpentinite mudflow mechanisms and sources: ODP drilling results on Mariana forearc seamounts. *Geochem. Geophys. Geosyst.* **7**, Q08014, doi:10.1029/2005GC001201.

German C. R. and Von Damm K. L. (2003) Hydrothermal processes. In *Treatise on Geochemistry* (eds. H. D. Holland and K. K. Turekian), **6**, pp. 181–222.

Gillis K. M., Coogan L. A. and Pedersen R. (2005) Strontium isotope constraints on fluid flow in the upper oceanic crust at the East Pacific Rise. *Earth Planet. Sci. Lett.* **232**, 83–94.

Hart S. R., Erlank A. J. and Kable E. D. J. (1974) Sea floor basalt alteration: some chemical and Sr isotopic effects. *Contrib. Mineral. Petrol.* **44**, 219–230.

Hattori K. and Guillot S. (2003) Volcanic fronts form as a consequence of serpentinite dehydration in the forearc mantle wedge. *Geology* **31**, 525–528.

Hershey J. P., Fernandez M., Milne P. J. and Millero F. J. (1986) The ionization of boric acid in NaCl, Na–Ca–Cl and Na–Mg–Cl solutions at 25 °C. *Geochim. Cosmochim. Acta* **50**, 143–148.

Ishikawa T. and Nakamura E. (1994) Origin of the slab component in arc lavas from across-arc variation of B and Pb isotopes. *Nature* **370**, 205–208.

Ildefonse B., Blackman D. K., John B. E., Ohara Y., Miller D. J., MacLeod C. J. and IODP Expeditions 304–305 Scientific Party (2007) Oceanic core complexes and crustal accretion at slow-spreading ridges. *Geology* **35**, 623–626.

Ishikawa T. and Tera F. (1999) Two isotopically distinct fluid components involved in the Mariana arc: evidences from Nb/B ratios and B, Sr, Nd, and Pb isotopes systematics. *Geology* **27**, 83–86.

Janecky D. R. and Seyfried, Jr., W. E. (1986) Hydrothermal serpentinization of peridotite within the oceanic crust: experimental investigations of mineralogy and major element chemistry. *Geochim. Cosmochim. Acta* **50**, 1357–1378.

Kakihana H., Kotaka M., Shohei S., Nomura M. and Okamoto N. (1977) Fundamental studies on ion-exchange separation of boron isotopes. *Bull. Chem. Soc. Jpn.* **50**, 158–163.

Karpoff A. M., Lagabrielle Y., Boillot G. and Girardeau J. (1989) L'authigenèse océanique de palygorskite par halmirolyse de péridotites serpentiniséees (Marge de Galice): ses implications géodynamiques. *C. R. Acad. Sci. Paris* **308**(Serie II), 1341–1348.

Karson J. A., Williams E. A., Früh-Green G. L., Kelley D. S., Yoerger D. R. and Jakuba M. (2006) Detachment Shear Zone on the Atlantis Massif Core Complex, Mid-Atlantic Ridge 30°N. *Geochem. Geophys. Geosys.* **7**(6), Q0601. doi:10.1029/2005GC001109.

Kawahata H. and Scott S. D. (1990) Strontium isotopes and water–rock interaction of the Agrokipia'B' stockwork deposit in the Troodos ophiolite, Cyprus: a fossil subseafloor ore body. *Geochem. J.* **24**, 349–356.

Kelley D. S., Karson J. A., Blackman D. K., Früh-Green G. L., Butterfield D. A., Lilley M. D., Olson E. J., Schrenk M. O., Roe K. K., Lebon G. T. and Rivizzigno P. A.AT3-60 Shipboard Party (2001) An off-axis hydrothermal vent field near the Mid-Atlantic Ridge at 30°N. *Nature* **412**, 145–149.

Kelley D. S., Karson J. A., Früh-Green G. L., Yoerger D., Shank T. M., Butterfield D. A., Hayes J. M., Schrenk M. O., Olson E., Proskuroski G., Jakuba M., Bradley A., Larson B., Ludwig K. A., Glickson D., Buckman K., Bradley A. S., Brazelton W. J., Roe K., Elend M., Delacour A. G., Bernasconi S. M., Lilley M. D., Baross J. A., Summons R. E. and Sylva S. P. (2005) A serpentinite-hosted ecosystem: the Lost City Hydrothermal Field. *Science* **307**, 1428–1434.

King R. L., Kohn M. J. and Eiler J. M. (2003) Constraints on the petrologic structure of the subduction zone slab–mantle interface from Franciscan Complex exotic ultramafic blocks. *Geol. Soc. Am. Bull.* **115**, 1097–1109.

Lagabrielle Y., Bideau D., Cannat M., Karson J. A. and Mével C. (1998) Ultramafic-,mafic plutonic rock suites exposed along the Mid-Atlantic Ridge (10°N-30°N). Symmetrical-asymmetrical distribution and implications for seafloor spreading processes. In *Faulting and Magmatism at Mid-Ocean Ridges*, *Geophys. Monogr. Ser.* **106** (eds. W. R. Buck, et al.). AGU, Washington, DC, pp. 153–176.

Leeman W. P. (1987) Boron geochemistry of volcanic arc magmas: evidence for recycling of subducted oceanic lithosphere. *EOS Trans. Am. Geophys. Union* **68**, 462.

Leeman W. P., Tonarini S., Chan L. H. and Borg L. E. (2004) Boron and lithium isotopic variations in a hot subduction zone—the southern Washington Cascades. *Chem. Geol.* **212**, 101–124.

Lemarchand D., Gaillardet J., Lewin E. and Allegre C. J. (2000) The influence of rivers on marine isotopes and implications for reconstructing past ocean pH. *Nature* **408**, 951–954.

Lister C. R. B. (1972) On the thermal balance of a mid-oceanic ridge. *Geophys. J. R. Astron. Soc.* **26**, 515–535.

Liu Y. and Tossell J. A. (2005) Ab initio molecular orbital calculations for boron isotope fractionations on boric acids and borates. *Geochim. Cosmochim. Acta* **69**, 3995–4006.

Ludwig K. A., Kelley D. S., Butterfield D. A., Nelson B. K. and Früh-Green G. L. (2006) Formation and evolution of carbonate chimneys at the Lost City Hydrothermal Field. *Geochim. Cosmochim. Acta* **70**, 3625–3645.

Macaulay C. I., Fallick A. E., Haszeldine R. S. and Graham C. M. (2000) Methods of laser-based stable isotope measurement applied to diagenetic cements and hydrocarbon reservoir quality. *Clay Minerals* **35**, 313–322.

Manning C. E. (2004) The chemistry of subduction-zone fluids. *Earth Planet. Sci. Lett.* **223**, 1–16.

McCulloch M. T., Gregory R. T., Wasserburg G. J. and Taylor H. P., Jr. (1980) A neodymium, strontium, and oxygen isotopic study of the Cretaceous Samail ophiolite and implications for the petrogenesis and seawater-hydrothermal alteration of oceanic crust. *Earth Planet. Sci. Lett.* **46**, 201–211.

McCulloch M. T., Gregory R. T., Wasserburg G. J., Taylor Jr. H. P. (1981) Sm–Nd, Rb–Sr, and O-18/ O-16 isotopic systematics in an oceanic crustal section; evidence from the Samail ophiolite. In *Oman Ophiolite* (eds. R. G. Coleman and C. A. Hopson). *J. Geophys. Res. B* **86**(4), 2721–2735.

Mesmer R. E., Baes C. F. and Sweeton F. H. (1972) Acidity measurements at elevated temperatures. VI. Boric acid equilibria. *Inorg. Chem.* **11**, 537–543.

Mesmer R. E., Marshall W. L., Palmer D. A., Simonson J. M. and Holmes H. F. (1988) Thermodynamics of aqueous association and ionization reactions at high temperatures and pressures. *J. Solut. Chem.* **17**, 699–718.

Mével C. (2003) Serpentinization of abyssal peridotites at mid-ocean ridges. *C. R. Geosci.* **335**, 825–852.

Michard A. and Albarede F. (1986) The REE content of some hydrothermal fluids. *Chem. Geol.* **55**, 51–60.

Michard A., Albarede F., Michard G., Minster J. F. and Charlou J. L. (1983) Rare-earth elements and uranium in high-temperature solutions from East Pacific Rise hydrothermal vent field (13°N). *Nature* **303**, 795–797.

Morris J. D. and Ryan J. G. (2003) Subduction zone processes and implications for changing composition of the upper and lower mantle. In *The Mantle and Core* (eds. H. D. Holland and K. K. Turekian). *Treatise on Geochemistry* **2**, pp. 451–471.

Morris J. D., Leeman W. P. and Tera F. (1990) The subducted component in island arc lavas: constraints from Be isotopes and B–Be systematics. *Nature* **344**, 31–36.

Muehlenbachs K. (1987) Alteration of the oceanic crust and the ^{18}O history of seawater. *Rev. Mineral.* **16**, 425–444.

Niu Y. (2004) Bulk-rock major and trace element compositions of abyssal peridotites: implications for mantle melting, melt extraction and post-melting processes beneath mid-ocean ridges. *J. Petrol.* **45**, 2423–2458.

Nooner S. L., Sasagawa G. S., Blackman D. K. and Zumberge M. A. (2003) Structure of oceanic core complexes: constraints from seafloor gravity measurements made at the Atlantis Massif. *Geophys. Res. Lett.* **30**, 1446. doi:10.1029/2003GL017126.

Oi T. (2000) Calculations of reduced partition function ratios of monomeric and dimeric boric acids and barates by the *ab initio* molecular orbital theory. *J. Nucl. Sci. Technol.* **37**, 166–172.

Pagani M., Lemarchand D., Spivack A. and Gaillardet J. (2005) A critical evaluation of the boron isotope-pH proxy: the accuracy of ancient ocean pH estimates. *Geochim. Cosmochim. Acta* **69**, 953–961.

Palmer M. R. (1991) Boron-isotope systematica of Hamahera arc (Indonesia) lavas: evidence for involvement of the subducted slab. *Geology* **19**, 215–217.

Palmer M. R. (1996) Hydration and uplift of the oceanic crust on the Mid-Atlantic Ridge associated with hydrothermal activity; evidence from boron isotopes. *Geophys. Res. Lett.* **23**, 3479–3482.

Palmer M. R. and Slack J. F. (1989) Boron isotopic composition of tourmaline from massive sulfide deposits and tourmalinites. *Contrib. Mineral. Petrol.* **103**, 434–451.

Palmer M. R. and Swihart G. H. (1996) Boron isotope geochemistry; an overview. In *Boron; mineralogy, petrology and geochemistry* (eds. E. S. Grew and L. M. Anovitz). *Rev. Mineral.* **33**, pp. 709–744.

Palmer M. R., Spivack A. J. and Edmond J. M. (1987) Temperature and pH controls over isotopic fractionation during adsorption of boron on marine clay. *Geochim. Cosmochim. Acta* **51**, 2319–2323.

Paulick H., Bach W., Godard M., De Hoog J. C. M., Suhr G. and Harvey J. (2006) Geochemistry of abyssal peridotites (Mid-Atlantic Ridge, 15°20′N, ODP Leg 209): implications for fluid/rock interaction in slow spreading environments. *Chem. Geol.* **234**, 179–210.

Proskurowski G., Lilley M. D., Kelley D. S. and Olson E. J. (2006) Low temperature volatile production at the Lost City Hydrothermal Field, evidence from a hydrogen stable isotope geothermometer. *Chem. Geol.* **229**, 331–343.

Ranero C. R., Phipps Morgan J., McIntosh K. and Reichert C. (2003) Bending-related faulting and mantle serpentinization at the Middle America trench. *Nature* **425**, 367–373.

Ranero C. R. and Sallarès V. (2004) Geophysical evidence for hydration of the crust and mantle of the Nazca plate during bending at the north Chile trench. *Geology* **32**, 549–552. doi:10.1130/G20379.1.

Rosner M., Erzinger J., Franz G. and Trumbull R. B. (2003) Slab-derived boron isotope signatures in arc volcanic rocks from the Central Andes and evidence for boron isotope fractionation during progressive slab dehydration. *Geochem. Geophys. Geosys.* **4**, 9005. doi:10.1029/2002GC000438.

Ryan J. G. and Langmuir C. H. (1993) The systematics of boron abundances in young volcanic rocks. *Geochim. Cosmochim. Acta* **57**, 1489–1498.

Saccocia P. J., Seewald J. S. and Shanks W. C. (2001) New D–H and ^{18}O–^{16}O fractionation factors for serpentine and talc from 250 to 450 °C. *Eos. Trans. AGU*, **82**(47), Fall Meet. Suppl., #V51B-0991 (abstr.).

Sakai R., Kusakabe M., Noto M. and Ishii T. (1990) Origin of waters responsible for serpentinization of the Izu–Ogasawara–Mariana forearc seamounts in view of hydrogen and oxygen isotope ratios. *Earth Planet. Sci. Lett.* **100**, 291–303.

Salters V. J. M. and Stracke A. (2004) Composition of the depleted mantle. *Geochem. Geophys. Geosys.* **5**. doi:10.1029/2003GC000597.

Savin S. M. and Lee M. (1988) Isotopic studies of phyllosilicates. In *Hydrous Phyllosilicates (Exclusive of Mica)* (ed. S. Bailey). *Rev. Mineral.* **19**, pp. 189–223.

Savov I. P., Rost D., Vicenzi D. and Zack T. (2006) Microscale mapping of boron and lithium in the Mariana sub-arc mantle via ToF-SIMIS. *Eos Trans. AGU*, **87**(36), Jt. Assem. Suppl., V43A-02.

Savov I. P., Ryan J. G., D'Antonio M., Kelley K. and Mattie P. (2005a) Geochemistry of serpentinized peridotites from the Mariana forearc conical seamount, ODP Leg 125: implications for the elemental recycling at subduction zones. *Geochem. Geophys. Geosys.* **6**. doi:10.1029/2004GC000777.

Savov, I. P., Guggino S., Ryan J. G., Fryer P. and Mottl M. J. (2005b) Geochemistry of serpentinite muds and metamorphic rocks from the Mariana forearc, ODP Sites 1200 and 778–779, South Chamorro and Conical Seamounts. In *Proceedings of ODP, Sci. Results* (M. Shinohara, M. H. Salisbury and C. Richter). Ocean Drilling Program, College Station, TX, **195** [Online].

Savov I. P., Ryan J. G., D'Antonio M. and Fryer P. (2007) Shallow slab fluid release across and along the Mariana arc-basin system: insights from geochemistry of serpentinized peridotites from the Mariana fore arc. *J. Geophys. Res.* **112**, B09205. doi:10.1029/2006JB004749.

Scambelluri M., Müntener O., Ottolini L., Pettke T. T. and Vannucci R. (2004) The fate of B, Cl and Li in the subducted oceanic mantle and in the antigorite-breakdown fluids. *Earth Planet. Sci Lett.* **222**, 217–234.

Schroeder T., John B. E. and Frost B. R. (2002) Geologic implications of seawater circulation through peridotite exposed at slow-spreading mid-ocean ridges. *Geology* **30**, 367–370.

Schroeder T. and John B. E. (2004) Strain localization on an oceanic detachment fault system, Atlantis Massif, 30°N, Mid-Atlantic Ridge. *Geochem. Geophys. Geosys.* **5**. doi:10.1029/2004GC000728.

Schwarcz H. P., Agyei E. K. and McMullen C. C. (1969) Boron isotopic fractionation during clay adsorption from seawater. *Earth Planet. Sci. Lett.* **6**, 1–5.

Seyfried, Jr., W. E. and Bischoff J. L. (1981) Experimental seawater–basalt interaction at 300 °C, 500 bars, chemical exchange, secondary mineral formation and implications for the transport of heavy metals. *Geochim. Cosmochim. Acta* **45**(2), 135–147.

Seyfried, Jr., W. E. and Dibble W. E. (1980) Seawater–peridotite interaction at 300 °C and 500 bars: implications for the origin of oceanic serpentinites. *Geochim. Cosmochim. Acta* **44**, 309–321.

Seyfried, Jr., W. E., Janecky D. R. and Mottl M. J. (1984) Alteration of the oceanic crust: implications for geochemical cycles of lithium and boron. *Geochim. Cosmochim. Acta* **48**, 557–569.

Seyler M., Cannat M. and Mével C. (2003) Evidence for major element heterogeneity in the mantle source of abyssal peridotites from the southwest Indian Ridge (52 to 68° East). *Geochem. Geophys. Geosys.* **4**, 9101. doi:10.1029/2002GC000305.

Shanks W. C. III (2001) Stable isotopes in seafloor hydrothermal systems: vent fluids hydrothermal deposits, hydrothermal alteration and microbial processes. In *Stable Isotope Geochemistry* (eds. J. W. Valley and D. R. Cole). *Rev. Mineral. Geochem.* **43**, pp. 469–525.

Sharp Z. D. (1990) A laser-based microanalytical method for the in situ determination of oxygen isotope ratios of silicates and oxides. *Geochem. Cosmochim. Acta* **54**, 1353–1357.

Sheppard S. M. F. (1980) Isotopic evidence for the origins of water during metamorphic processes in oceanic crust and ophiolite complexes. In *Colloque Internationau du C.N.R.S Association mafiques ultra-mafiques dans les orogénes* **272**, pp. 135–147.

Simon L., Lécuyer C., Maréchal C. and Coltice N. (2006) Modelling the geochemical cycle of boron: implications for the long-term δ^{11}B evolution of seawater and oceanic crust. *Chem. Geol.* **225**, 61–76.

Smith D. K., Cann J. R. and Escarin J. (2006) Widespread active detachment faulting and core complex formation near 13°N on the Mid-Atlantic Ridge. *Nature* **442**, 440–443.

Smith H. J., Spivack A. J., Staudigel H. and Hart S. R. (1995) The boron isotopic composition of altered oceanic crust. In *The Mantle–Ocean Connection* (eds. H. Staudigel, F. Albarede, D. Hilton and T. Elliott) *Chem. Geol.* **126**(2), pp. 119–135.

Sogalevich A., Bogdanov Y., Bortnikov N., Silantyev S., Galkin S., Lein, A. and Shipboard Party (2005) A comparative study of MAR hydrothermal fields found in different geodynamic settings: preliminary results of the 50th cruise (August–September 2005) of R/V Akademik Mstislav Keldysh. *InterRidge News* **14**, 16–18.

Spivack A. J. and Edmond J. M. (1987) Boron isotope exchange between seawater and oceanic crust. *Geochim. Cosmochim. Acta* **51**, 1033–1043.

Straub S. M. and Layne G. D. (2002) The systematics of boron isotopes in Izu arc front volcanic rocks. *Earth Planet. Sci. Lett.* **198**, 25–39.

Spivack A. J., Palmer M. R. and Edmond J. M. (1987) The sedimentary cycle of the boron isotopes. *Geochim. Cosmochim. Acta* **51**, 1939–1949.

Taylor, Jr., H. P. (1974) The application of oxygen and hydrogen isotope studies to problems of hydrothermal alteration and ore deposition. *Econ. Geol.* **69**, 843–883.

Taylor H. P. (1977) Water/rock interactions and the origin of H_2O in granitic batholiths. *J. Geol. Soc. Lond.* **133**, 509–558.

Tenthorey E. and Hermann J. (2004) Composition of fluids during serpentinite breakdown in subduction zones: evidence for limited boron mobility. *Geology* **32**, 865–868.

Tonarini S., Pennisi M. and Leeman W. P. (1997) Precise boron isotopic analysis of complex silicate (rock) samples using alkali carbonate fusion and ion-exchange separation. *Chem. Geol.* **142**, 129–137.

Tonarini S., Agostini S., Doglioni C., Innocenti F. and Manetti P. (2007) Evidence for serpentinite fluid in convergent margin systems: the example of El Salvador (Central America) arc lavas. *Geochem. Geophys. Geosys.* **8**, Q09014. doi:10.1029/2006GC001508.

Tonarini S., Pennisi M., Adorni-Braccesi A., Dini A., Ferrara G., Gonfiantini R., Wiedenbeck M. and Gröning M. (2003) Intercomparison of boron isotope and concentration measurements. Part I: selection, preparation and homogeneity tests of the intercomparison materials. *Geostand. Newsl.* **27**, 21–39.

Thompson G. and Melson W. G. (1970) Boron contents of serpentinites and metabasalts in the oceanic crust: implications for the boron cycle in the oceans. *Earth Planet. Sci. Lett.* **8**, 61–65.

Turner S., Tonarini S., Bindeman I., Leeman W. P. and Schaefer B. F. (2007) Boron and oxygen isotope evidence for recycling of subducted components over the past 2.5 Gyr. *Nature* **447**, 702–705.

Ulmer P. and Trommsdorff V. (1995) Serpentine stability to mantle depths and subduction-related magmatism. *Science* **268**, 858–861.

Wenner D. B. and Taylor H. P. (1973) Oxygen and hydrogen isotope studies of the serpentinization of ultramafic rocks in the oceanic environments and continental ophiolite complexes. *Am. J. Sci.* **273**, 207–239.

Wetzel L. R. and Schock E. L. (2000) Distinguishing ultramafic- from basalt-hosted submarine hydrothermal systems by comparing calculated vent fluid compositions. *J. Geophys. Res.* **105**(B4), 8319–8340.

Wheat C. G. and Mottl M. J. (2004) Geochemical fluxes through mid-ocean ridge flanks. In *Hydrogeology of the Oceanic Lithosphere* (eds. E. E. Davis and H. Elderfield). Cambridge University Press, pp. 627–658.

Williams L. B., Hervig R. L., Holloway J. R. and Hutcheon I. (2001) Boron isotope geochemistry during diagenesis. Part I. Experimental determination of fractionation during illitization of smectite. *Geochim. Cosmochim. Acta* **65**, 1769–1782.

Wofford W. T., Gloyna E. F. and Johnston K. P. (1998) Boric acid equilibria in near-critical and supercritical water. *Ind. Eng. Chem. Res.* **37**, 2045–2051.

Workman R. K. and Hart S. R. (2005) Major and trace element composition of the depleted MORB mantle (DMM). *Earth Planet. Sci. Lett.* **231**, 53–72.

Wunder B., Meixner A., Romer R. L., Wirth R. and Heinrich W. (2005) The geochemical cycle of boron: constraints from boron isotope partitioning experiments between mica and fluid. *Lithos* **84**, 206–216.

Yagasaki T., Iwahashi K., Saito S. and Ohmine I. (2005) A theoretical study on anomalous temperature dependance of pK_w of water. *J. Chem. Phys.* **122**, 144504/9.

You C. F., Chan L. H., Spivack A. J. and Gieskes J. M. (1995) Lithium, boron, and their isotopes in sediments and pore waters of Ocean Drilling Program Site 808, Nankai Trough: Implications for fluid expulsion in accretionary prisms. *Geology* **23**, 37–40.

You C. F., Spivack A. J., Gieskes J. M., Martin J. B. and Davisson M. L. (1996) Boron contents and isotopic compositions in pore water: a new approach to determine temperature-induced artifacts—geochemical implications. *Mar. Geol.* **129**, 351–361.

Zeebe R. E. (2005) Stable boron isotope fractionation between dissolved $B(OH)_3$ and $B(OH)_4^-$. *Geochim. Cosmochim. Acta* **69**, 2753–2766.

Zheng Y. F. (1993) Calculation of oxygen-isotope fractionation in hydroxyl-bearing silicates. *Earth Planet. Sci. Lett.* **120**, 247–263.

Associate editor: Jeffrey C. Alt